Part III Project:

Instanton calculations of tunnelling in water clusters

(Extended version)

Michael F. Herbst
info@michael-herbst.com

Girton College
University of Cambridge

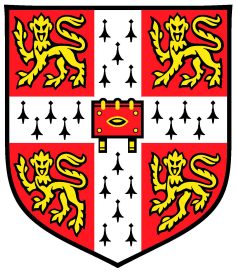

26th April 2013

Declaration

This dissertation is submitted in partial fulfilment of the requirements for Part III Chemistry. It describes work carried out in the Department of Chemistry in the Michaelmas Term 2012 and the Lent Term 2013. Unless otherwise indicated, the research described is my own and not the product of collaboration.

Michael F. Herbst
(26^{th} April 2013)

Acknowledgements

A special thanks to

- the whole Althorpe group, especially my day-to-day supervisor Adam Reid and Stuart Althorpe, for their excellent support throughout.
- Jeremy Richardson for answering all of my numerous questions either via email or in person and for various tips and suggestions.

Licensing and redistribution

To my parents, God and the world.

Abstract

This work makes use of the ring-polymer instanton method to calculate tunnelling splittings in an isomer of the water decamer called PP2, the enneakaidecamer (19mer) and the icosamer (20mer) clusters. A detailed discussion of the numerical implementation and some computational strategies used throughout the work is given, following a brief summary of the ring-polymer instanton method itself.

For the investigation of tunnelling in the PP2 isomer of the water decamer the computationally expensive, but accurate WHBB potential from the Bowman group is used. Due to the symmetry of this system, calculation of a single instanton is enough to predict the tunnelling splitting pattern in the high resolution tetraherz laser vibration-rotation-tunnelling spectrum.

Next a comparison of the cheaper TTM3-F potential with two more accurate potentials from the Bowman group, WHBB and HBB2, is made based on instanton calculations in the water decamer and dimer. The TTM3-F values were never out by more than an order of magnitude such that the kink path weights obtained using TTM3-F can be safely used to distinguish important from unimportant tunnelling paths. This becomes especially relevant for larger clusters where calculations using the TTM3-F potential are considerably faster than their equivalents using the Bowman potentials.

Finally we consider some examples of instantons in the water 19mer and 20mer where all calculations are done solely using the TTM3-F potential. The rigidity of the clusters and the small resulting kink path weights lead to the conclusion that tunnelling is very unlikely to be experimentally observable for both these clusters.

Contents

List of Tables

List of Figures

List of Abbreviations and Important Symbols

β	Thermodynamic beta, $\beta = \frac{1}{k_\mathrm{B}T}$ with Boltzmann constant k_B
β_N	Beta per bead, $\beta_N = \frac{\beta}{N}$ with N being the number of beads
Δ	The tunnelling splitting of a double well system (see section 2.1.1 on page 4)
$\mathbf{i}$	Complex unit, $\mathbf{i}^2 = -1$
$\int_{-\infty}^{\infty} \mathrm{d}\underline{\boldsymbol{x}}$	Lazy expression equivalent to $\int_{-\infty}^{\infty} \mathrm{d}x_1 \int_{-\infty}^{\infty} \mathrm{d}x_2 \cdots \int_{-\infty}^{\infty} \mathrm{d}x_N$ for N being the number of sampling points / beads; introduced in (2.3) on page 7
$\mathbf{W}$	tunnelling matrix introduced in section 2.3 on page 17
S_kink	Action of a single kink (see (2.12) of page 12)
ε	Gradient threshold for the minimisation (see section 3.1 on page 19)
a_0	Bohr radius, $a_0 = 0.52918\,\text{Å}$
E_H	Hartree energy, $E_H = 27.211\,\mathrm{eV}$
$h_{\lambda\mu}$	kink path weight (see (2.26) on page 18)
TTM3-F	Cheap potential by Fanourgakis and Xantheas [1]
HBB2	Older Bowman potential [2]
L-BFGS	The limited memory Broyden-Fletcher-Goldfarb-Shanno minimisation algorithm [3]
PES	Potential energy surface
RPI	Ring-polymer instanton

VRT	High-resolution terahertz laser vibration-rotation-tunnelling spectroscopy
WHBB	Newer Bowman potential [4]

Chapter 1

Motivation

Tunnelling is the quantum-mechanical phenomenon of a particle propagating through a barrier, which it could not traverse based on purely classical considerations. It plays an important role in the understanding of physical processes happening on a molecular and submolecular scale and hence has implications for the chemical properties of matter as well.

The first experimental evidence for tunnelling goes back to the discovery of radioactivity by Henri Becquerel and Marie and Pierre Curie at the turn of the 20th century. The full connection between radioactive decay and tunnelling was only made 30 years later by George Gamow in 1928 [5] — just a year after Hund published a paper positing the idea of tunnelling [6].

In the field of high resolution spectroscopy tunnelling effects often need to be taken into account in order to understand the resulting spectrum. In the high resolution microwave spectrum of ammonia, for example, an extra splitting of lines due to the presence of inversion tunnelling along the umbrella-type normal mode is observed [7]. Similarly the torsional tunnelling in ethylene gives rise to a splitting of lines. The pattern, however, is more complicated [8]. Measuring these splittings is experimentally convenient — Cleeton and Williams [7], for example, did their measurement at room temperature and atmospheric pressure.

1.1 Assessment of water potential energy surfaces based on tunnelling splittings

Water clusters are considerably less stable than ammonia or ethylene. All spectroscopic measurements on these molecules hence need to be done at much lower temperatures and pressures. Nevertheless reliable experimental data has been obtained for a variety of small water clusters in recent years by high-resolution terahertz laser vibration-rotation-tunnelling spectroscopy (VRT) [9].

These data play a key role in assessing the accuracy of the large number of potentials that have been developed for the modelling of water [9]. Even though the behaviour of water molecules is different in bulk water compared to clusters [10], the properties of the bulk may often be predicted accurately using potentials that contain only pairwise and three-body terms [1, 11, 12]. Furthermore according to Bukowski et al. [13] the calculated tunnelling splittings are extremely sensitive to details like the shape of the potential energy surface (PES) away from the local minima and may provide information about, for example, the short-range anisotropy of the potential [13]. By comparing experimental and computational tunnelling splittings we are hence able to judge how accurately a PES describes the 2-body and 3-body terms. Doing this with bulk properties is harder — especially in the low temperature regime — since the calculation of macroscopic quantities involves averaging over a larger portion of configuration space than it is the case with tunnelling splitting calculations. Available experimental data is furthermore less detailed and prim.

1.2 Calculating tunnelling splittings

Out of the large number of methods available for the calculation of tunnelling splittings [10, 14] this work makes use of the Ring Polymer Instanton (RPI) method developed by Richardson and Althorpe [14]. As the authors point out, an advantage of the RPI approach is that solving the Schrödinger equation is not required. Doing this exactly or even approximately would only be possible for the smallest systems. Neither does it require a large sampling of configuration space, like diffusion Monte Carlo [15] or other Path Integral approaches [16] would. Instead, sampling the PES along a single path between each pair of local minima is sufficient. Compared to other such “one-shot” methods like the Wentzel-Kramers-Brillouin approach [17] we furthermore do not need to specify the tunnelling path *a priori*. This would become especially difficult for the larger water clusters we will consider in this work. To date the RPI method

is the only method that successfully computed tunnelling splittings for water clusters larger than the trimer [18].

An outline of the derivation of the RPI method is given in chapter 2. Chapter 3 focuses on the numerical implementations and some strategies followed to calculate splittings.

1.3 Potentials used for the splitting calculations

The calculations presented in this work were either carried out using the widely-used TTM3-F potential developed by Fanourgakis and Xantheas [1] or the WHBB [4] potential — the most recent of a series of potentials from the Bowman group. Previous RPI calculations on the tunnelling in water dimer and trimer by Richardson et al. [10] showed that the tunnelling splittings obtained from calculations using HBB2 [2] — an older Bowman potential — yielded good agreement with experiment whereas TTM3-F was computationally cheaper, but the agreement less good. This suggests that TTM3-F is a good example for a crude potential, whereas the Bowman potential WHBB is both more accurate and more expensive.

Compared to the previously published RPI calculations [10, 19] the water clusters studied here are larger. In chapter 4 we will calculate the tunnelling splittings in the PP2 isomer of the water decamer using the WHBB potential. Chapter 5 then presents a comparison of the TTM3-F and Bowman potentials both based on the decamer results as well as instanton calculations in the water dimer. In chapter 6 tunnelling in the water enneakaidecamer (19mer) and icosamer (20mer) is considered briefly using the cheaper TTM3-F PES.

Chapter 2

Ring-polymer instanton theory

In this chapter we outline the derivation of RPI theory in the case of tunnelling between two symmetric wells. We will furthermore attempt to rationalise the results for more general cases of higher dimensions and more wells.

2.1 Tunneling between two symmetric wells

2.1.1 The tunnelling splitting Δ

Consider as a first model system the double well potential $V(x) = \lambda(x^2 - x_0^2)^2$. If we first assume that the barrier between the minima at $\pm x_0$ is high enough such that tunnelling can be neglected both wells are essentially independent from another. We can approximate both sides of the potentials by harmonic wells $V_L(x) = 4x_0\lambda^2(x + x_0)^2$ and $V_R(x) = 4x_0\lambda^2(x - x_0)^2$ centered around $-x_0$ and $+x_0$, respectively, as indicated by the dashed parabola in fig. 2.1 on page 6. The solutions to the Schrödinger equation in the harmonic wells give us their respective ground states as the Gaussians Ψ_L and Ψ_R (see fig. 2.1) [20]. Since the wells are related by symmetry (about $x = 0$) their ground states are obviously degenerate with energy E_0.

Allowing tunnelling to occur the LHS and RHS wells are no longer isolated; rather the states of both wells are able to interact through the barrier. Reid [20] approximated the resulting lowest energy states by Variational Principles using a linear combination of the harmonic ground states of the non-tunnelling system Ψ_L and Ψ_R, which yields fig. 2.2 on page 6. In comparison to fig. 2.1 we could think of tunnelling as if it splits the degenerate ground state apart

into the two states Ψ_+ and Ψ_-, separated by an energy difference Δ — the *tunnelling splitting*.

2.1.2 Relation of Δ to the partition function of the system

In the limit of low temperature, i.e. large $\beta = \frac{1}{k_B T}$, we can assume that only the lowest energy states contribute significantly to the partition function of the systems. Taking $Q(\beta)$ and $Q_0(\beta)$ to be the partition function in the tunnelling and non-tunnelling cases, respectively, allows us to write in this limit [14]

$$\begin{aligned}\frac{Q(\beta)}{Q_0(\beta)} &= \frac{\sum_i \exp\left(-\beta\tilde{E}_i\right)}{\sum_i \exp\left(-\beta E_i\right)} \\ &\simeq \frac{\exp\big(-\beta(E_0-\Delta/2)\big)+\exp\big(-\beta(E_0+\Delta/2)\big)}{2\exp\left(-\beta E_0\right)} \\ &= \cosh\left(\frac{\beta\Delta}{2}\right), \end{aligned} \tag{2.1}$$

where $\tilde{E}_i$ and E_i denote the energy states in the tunnelling and non-tunnelling systems, respectively.

2.1.3 The discretised Feynman path integral expression for a single particle partition function

Using the alternative formulation of the partition function in terms of the trace of the quantum Boltzmann operator [14, 21]

$$Q(\beta) = \mathrm{tr}\left(\exp\left(-\beta\hat{\mathrm{H}}\right)\right) = \int_{-\infty}^{\infty} \mathrm{d}x \ \left\langle x\middle|\exp\left(-\beta\hat{\mathrm{H}}\right)\middle|x\right\rangle \tag{2.2}$$

we can apply the Trotter theorem to give [20, 22]

$$Q(\beta) = \lim_{N\to\infty}\int_{-\infty}^{\infty} \mathrm{d}x \ \left\langle x\middle|\hat{\Omega}^N\middle|x\right\rangle$$

with

$$\hat{\Omega} = \exp\left(-\frac{\beta}{2N}\hat{\mathrm{V}}\right)\exp\left(-\frac{\beta}{N}\hat{\mathrm{T}}\right)\exp\left(-\frac{\beta}{2N}\hat{\mathrm{V}}\right).$$

where $\hat{\mathrm{V}}$ denotes the potential and $\hat{\mathrm{T}}$ the kinetic part of the Hamiltonian $\hat{\mathrm{H}} = \hat{\mathrm{T}} + \hat{\mathrm{V}}$. Making use of the completeness of the coordinate basis we can insert $N-1$ factors of

$$1 = \int_{-\infty}^{\infty} \mathrm{d}x_i \ |x_i\rangle\langle x_i|$$

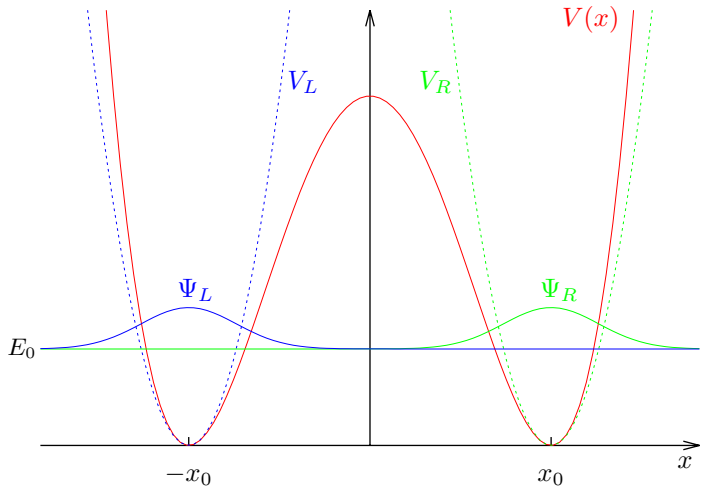

Figure 2.1: Schematic illustration of the two degenerate ground states Ψ_R and Ψ_L of a double well potential of the form $V(x) = \lambda(x^2 - x_0^2)^2$ when tunnelling is not taken into account. The dashed lines indicate the harmonic approximations $V_R(x) = 4x_0\lambda^2(x - x_0)^2$ and $V_L(x) = 4x_0\lambda^2(x + x_0)^2$ around the minima. (Figure based on Reid [20])

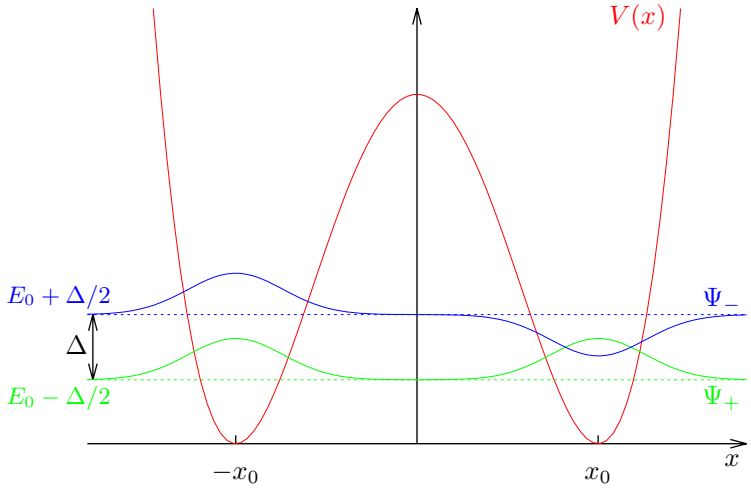

Figure 2.2: Illustration of the potential $V(x)$ of fig. 2.1 with tunnelling effects considered. Shown are the two lowest energy states Ψ_+ and Ψ_- (solid lines) and respective energies (dashed lines) separated by the tunnelling splitting Δ. (Figure based on Reid [20])

between each pair of $\hat{\Omega}$, which yields [20]

$$\begin{aligned} Q(\beta) &= \lim_{N\to\infty} \int_{-\infty}^{\infty} \mathrm{d}x_1 \int_{-\infty}^{\infty} \mathrm{d}x_2 \cdots \int_{-\infty}^{\infty} \mathrm{d}x_N \prod_{i=1}^{N} \left\langle x_i \middle| \hat{\Omega} \middle| x_{i+1} \right\rangle \\ &\equiv \lim_{N\to\infty} \int_{-\infty}^{\infty} \mathrm{d}\underline{\boldsymbol{x}} \prod_{i=1}^{N} \left\langle x_i \middle| \hat{\Omega} \middle| x_{i+1} \right\rangle \end{aligned} \tag{2.3}$$

where $x = x_1 = x_{N+1}$ and

$$\underline{\boldsymbol{x}} = \begin{pmatrix} x_1 \\ x_2 \\ \vdots \\ x_N \end{pmatrix}.$$

It can be shown [20, 22] that the latter expression (2.3) can be further manipulated to [14]

$$Q(\beta) = \lim_{N\to\infty} \left(\frac{1}{2\pi\beta_N\hbar^2} \right)^{\frac{N}{2}} \int_{-\infty}^{\infty} \mathrm{d}\underline{\boldsymbol{x}} \, \exp\left[-\beta_N U_N(\beta, \underline{\boldsymbol{x}})\right] \tag{2.4}$$

with

$$U_N(\beta, \underline{\boldsymbol{x}}) = \left[\sum_{i=1}^{N} V(x_i) + \frac{(x_{i+1} - x_i)^2}{2\left(\beta_N\hbar\right)^2} \right]_{x_{N+1}=x_1} \tag{2.5}$$

as well as $\beta_N = \beta/N$.

2.1.4 The relation of U_N to the discretised action S_N in imaginary time

Comparing the quantum Boltzmann operator $\exp\left(-\beta\hat{\mathrm{H}}\right)$ of (2.2) to the quantum time evolution operator $\exp\left(-\mathbf{i}\,\frac{\hat{\mathrm{H}}t}{\hbar}\right)$ we get the relation

$$t = -\mathbf{i} \underbrace{\beta\hbar}_{=:\tau},$$

which implies that the propagator of a system with respect to imaginary time $\tau = \mathbf{i}\,t$ will resemble the partition function upon taking the trace. This means that applying the mathematical trick of rotating the time axis, along which we evolve the system, by $\pi/2$ in the complex time plane, we can obtain quantities related to the partition function[1]. For example consider a particle of mass m moving periodically in a turned over potential $-V(x)$ with imaginary period τ.

[1] For a more detailed discussion of imaginary time see Reid [20] and Shankar [23].

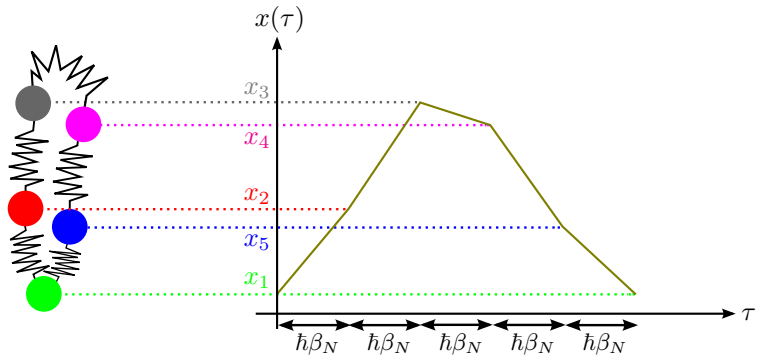

Figure 2.3: Illustration of a five-bead ring polymer on the left and the corresponding evolution of a particle $x(\tau)$ in imaginary time on the RHS. Note how each bead is a snapshot of the initial particle propagated in imaginary time by an integer number of imaginary-time slices $\hbar\beta_N$. (Based on Reid [20])

In mass scaled coordinates $x(\tau) = \sqrt{m} \times \textit{position}$ the action in imaginary time is

$$S = \int_0^\tau \mathrm{d}\tau' \;\; V\big(x(\tau')\big) + \frac{1}{2}\left(\frac{\mathrm{d}x(\tau')}{\mathrm{d}\tau'}\right)^2 \qquad \text{with } x(0) = x(\tau)$$

and in a discretised form of N time slices of width $\tau/N = \hbar\beta_N$, such that $x_{j+1} = x(j \cdot \hbar\beta_N)$ and $x_{N+1} = x_1$ we get [20]

$$S_N = \hbar\beta_N \left(\sum_{j=1}^{N} V(x_j) + \frac{(x_{j+1} - x_j)^2}{2\,(\beta_N \hbar)^2} \right).$$

Comparison with (2.5) yields

$$S_N(\beta, \underline{\boldsymbol{x}}) = \hbar\beta_N U_N(\beta, \underline{\boldsymbol{x}}). \tag{2.6}$$

2.1.5 U_N as the ring-polymer potential

One can further show [20] that equations (2.4) and (2.5) have the form of a classical partition function of a set of beads connected by harmonic springs (LHS of fig. 2.3). Using the concept of imaginary time introduced above we can understand the beads to be snapshots of the initial system taken after an integer number of imaginary-time intervals $\hbar\beta_N$ (see RHS of fig. 2.3). The frequencies of the springs are all equal to $\frac{1}{\hbar\beta_N}$, implying that the stiffness is temperature dependant. Since the nature of the partition function requires this object to be a closed ring, one also calls it a *ring polymer* and consequently refers to $U_N(\beta, \underline{\boldsymbol{x}})$ as the *ring-polymer potential*.

2.1.6 Approximate evaluation of Q in (2.4)

So far the expression (2.4) on page 7 is exact in the limit of large β and N. Choosing sufficiently large values for these quantities would in principle allow us to calculate the partition function directly with an acceptable accuracy. For such a large N, however, a N-dimensional numeric integration is still extremely expensive. Fortunately the integrand in (2.4) becomes very small for large $U_N(\beta, \underline{\boldsymbol{x}})$. We can hence apply a so-called *steepest descent* approximation, where only the regions of $U_N(\beta, \underline{\boldsymbol{x}})$ close to its respective minima $\underline{\tilde{\boldsymbol{x}}}^M$ are considered.

The condition for $\underline{\tilde{\boldsymbol{x}}}^M$ being a minimum of $U_N(\beta, \underline{\boldsymbol{x}})$

$$\left.\frac{\partial U_N(\beta, \underline{\boldsymbol{x}})}{\partial x_i}\right|_{\underline{\boldsymbol{x}}=\underline{\tilde{\boldsymbol{x}}}^M} = 0$$

lets us expand $U_N(\beta, \underline{\boldsymbol{x}})$ about the minimum $\underline{\tilde{\boldsymbol{x}}}^M$ to a second order Taylor series:

$$U_N(\beta, \underline{\boldsymbol{x}}) \simeq U_N(\beta, \underline{\tilde{\boldsymbol{x}}}^M) + \frac{1}{2}\sum_{i=1}^{N}\sum_{j=1}^{N}(x_i - \tilde{x}_i^M)G_{ij}^M(x_j - \tilde{x}_j^M)$$

According to Reid [20] we can evaluate the Hessian about minimum M as

$$G_{ij}^M = \left.\frac{\partial^2 U_N(\beta, \underline{\boldsymbol{x}})}{\partial x_i \partial x_j}\right|_{\underline{\boldsymbol{x}}=\underline{\tilde{\boldsymbol{x}}}^M} = V''(\tilde{x}_i^M)\delta_{ij} - \frac{\delta_{i,j-1} - 2\delta_{ij} + \delta_{i,j+1}}{(\hbar\beta_N)^2}.$$

This can be done for each of the minima allowing us to rewrite (2.4) (in the approximation) as

$$\begin{aligned} Q(\beta) \simeq \lim_{N\to\infty} \left(\frac{1}{2\pi\beta_N\hbar^2}\right)^{\frac{N}{2}} \sum_{\text{minima } M} \exp\left(-\beta_N U_N(\beta, \underline{\tilde{\boldsymbol{x}}}^M)\right) \\ \cdot \int_{-\infty}^{\infty} \mathrm{d}\underline{\boldsymbol{x}} \, \exp\left(-\frac{\beta_N}{2}\sum_{i=1}^{N}\sum_{j=1}^{N}(x_i - \tilde{x}_i^M)G_{ij}^M(x_j - \tilde{x}_j^M)\right). \end{aligned} \tag{2.7}$$

2.1.7 Changing (2.7) to normal-mode coordinates

Diagonalisation of the Hessian matrix

$$\mathbf{G}^M \underline{\boldsymbol{s}}^{M(i)} = \left(\eta_i^M\right)^2 \underline{\boldsymbol{s}}^{M(i)}$$

gives us a set of N normalised eigenvectors $\underline{\boldsymbol{s}}^{M(i)}$ — the *normal modes*. Their associated eigenfrequencies are denoted by η_i^M.

According to Reid [20] the integrals in (2.7) can be greatly simplified if normal-mode coordinates s_i^M are used. Transforming the basis appropriately yields a product of Gaussian integrals

$$Q(\beta) \simeq \lim_{N\to\infty} \left(\frac{1}{2\pi\beta_N\hbar^2}\right)^{\frac{N}{2}} \sum_{\text{minima } M} \exp\left(-\beta_N U_N(\beta, \underline{\tilde{\boldsymbol{x}}}^M)\right) \cdot \prod_{i=1}^{N} \int_{-\infty}^{\infty} \mathrm{d}s_i^M \ \exp\left(-\frac{\beta_N}{2}\left(\eta_n^M\right)^2 \left(s_i^M\right)^2\right),$$

which can be Evaluated to give [14]

$$Q(\beta) \simeq \tilde{Q}(\beta) = \left(\frac{1}{\beta_N\hbar}\right)^N \sum_{\text{minima } M} \frac{1}{\sqrt{\det \mathbf{G}^M}} \exp\left(-\beta_N U_N(\beta, \underline{\tilde{\boldsymbol{x}}}^M)\right) \tag{2.8}$$

in the limit of large N and β.

2.1.8 Periodic orbits and kinks

In section 2.1.4 on page 7 we saw that the action of periodic motions in the inverted potential $-V$ and the ring-polymer potential are related by (2.6). This implies that the minima $\underline{\tilde{\boldsymbol{x}}}$ of $U_N(\beta, \underline{\boldsymbol{x}})$ are also minimising the action of a periodic path $\underline{\boldsymbol{x}}$ in imaginary time, which makes them *periodic orbits*.

Non-tunnelling system

For a system of two symmetric wells, which are not interacting via tunnelling, there are only two possible orbits: All beads are located at the bottom of one well only. Due to symmetry the determinants of the Hessian matrices at both minima are identical to a common $\det \mathbf{G}_0$ and we get using (2.8) [14]

$$\tilde{Q}_0(\beta) = \left(\frac{1}{\hbar\beta_N}\right)^2 \frac{2}{\sqrt{\det \mathbf{G}_0}} \tag{2.9}$$

Full system

Apart from the non-tunnelling orbits given above the full system also comprises an infinite number of orbits in which the particles move back and fourth between the two minima. As fig. 2.4 suggests most beads are, however, still stationary at one of the minima. The moves between the minima — the so-called *kinks* — are very rapid, meaning that only very few beads participate in them. Due to the closed ring nature of the orbits only even numbers of kinks in an orbit are possible.

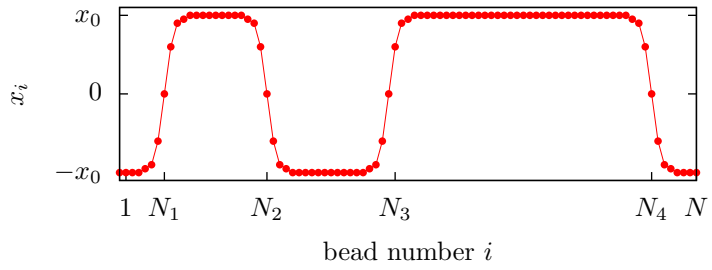

Figure 2.4: A 4-kink trajectory starting and ending at $-x_0$. The kinks may be distinguished from one another by the number of the central bead N_1, N_2, N_3, N_4. (Based on Richardson and Althorpe [14])

Having established the concept of a kink we can re-express (2.8) of page 10 as

$$\tilde{Q}(\beta) = \tilde{Q}_0(\beta) + \sum_{N_1,N_2} \tilde{Q}_2(N_1,N_2|\beta) + \sum_{N_1,N_2,N_3,N_4} \tilde{Q}_4(N_1,N_2,N_3,N_4|\beta) + \cdots + \sum_{N_1,N_2,\ldots,N_4} \tilde{Q}_n(N_1,N_2,\ldots,N_n|\beta) + \cdots , \tag{2.10}$$

where $\tilde{Q}_n(N_1,N_2,\ldots,N_n|\beta)$ is the contribution from an n-kink minimum and $N_1,N_2,\ldots,N_n$ are the bead indices at the centres of the kinks (cf. 2.4). The number of terms in each of the sums is $\frac{2N^n}{n!}$ [14].

2.1.9 Zero frequency modes

So far we have neglected that each n-kink minimum possesses n modes of very low frequency, which tend to zero in the limit $\hbar\beta_N \to 0$ [14]. To these so-called *zero-frequency modes* the steepest decent approximation we used in section 2.1.6 on page 9 cannot be applied. Instead we need to treat their contributions to Q seperately. The net result[2] is that for each n-kink minimum in (2.10) we must replace the determinant term in (2.8),

$$\frac{1}{\sqrt{\det \mathbf{G}^M}},$$

by the term

$$\left(\frac{S_{\text{kink}}}{2\pi\hbar}\right)^{n/2} \frac{(\hbar\beta_N)^n}{\sqrt{(\det \mathbf{G}^M)'}} \tag{2.11}$$

[2]For details consider Reid [20].

where $\sqrt{(\det \mathbf{G}^M)'}$ denotes the product of all eigenfrequencies η_i^M except the ones corresponding to zero-frequency modes. Furthermore we define S_{kink} as the (discretised) action of a single kink:

$$S_{\text{kink}} = \sum_{i \in \text{kink}} \frac{(\tilde{x}_{i+1} - \tilde{x}_i)^2}{\hbar \beta_N} \tag{2.12}$$

where the sum is running over all beads of the kink.

2.1.10 Describing kinks using a linear polymer

Factorising the ring-polymer potential into kinks

As indicated above, most beads of the ring polymer are stationary at $\pm x_0$. In the large N limit the individual kinks are hence separated by such a large number of these stationary beads that the kink movements are independent from one another. If the external potential V is furthermore zeroed such that $V(\pm x_0) = 0$, the stationary beads do not contribute to the sum in (2.19) on page 15 at all. Hence U_N factors into kinks, eg. for an n-kink minimum

$$U_N(\beta, \underline{\tilde{\boldsymbol{x}}}^M) = n U_{\text{kink}} = \frac{n S_{\text{kink}}}{\hbar \beta_N}.$$

Here U_{kink} denotes the contribution of the beads involved in the kink to the potential $U_N(\beta, \underline{\tilde{\boldsymbol{x}}}^M)$.

The linear polymer potential

Similar to the case of a ring polymer, one is also able to consider a linear string of system replicas connected by Hooke's Law springs of frequency $\frac{1}{\hbar \beta_N}$. If the start and end is connected to the minima $\pm x_0$ a *fixed-ended linear polymer* subject to the potential

$$U_L(\beta, \underline{\boldsymbol{x}}) = \sum_{i=1}^{L} V(x_i) + \frac{1}{2(\hbar \beta_N)^2} \left((x_1 + x_0)^2 + \sum_{i=1}^{L-1} (x_{i+1}) - x_i)^2 + (x_0 - x_L)^2 \right)$$

results. The single kink minima $\underline{\tilde{\boldsymbol{x}}}^{n=1}$ of such a polymer can be used to represent a single kink trajectory between the minima at $\pm x_0$. In the limit of large N and L we get the exact relationship

$$U_L(\beta, \underline{\tilde{\boldsymbol{x}}}^{n=1}) = U_{\text{kink}} = \frac{S_{\text{kink}}}{\hbar \beta_N}. \tag{2.13}$$

Usually one refers to these minima $\underline{\tilde{\boldsymbol{x}}}^{n=1}$ of the linear polymer as *instantons*[3].

2.1.11 Finding the tunnelling splitting

The partition function $\tilde{Q}(\beta)$ in terms of the linear polymer

Combining the results of the previous section with equations (2.8) and (2.11) allows us to state [20]

$$\tilde{Q}(\beta) = \left(\frac{1}{\beta_N \hbar}\right)^N \sum_{\text{minima } M} \left(\frac{\beta_N U_L(\beta, \underline{\tilde{\boldsymbol{x}}}^{n=1})}{2\pi}\right)^{n/2} \frac{(\hbar\beta_N)^n}{\sqrt{(\det \mathbf{G}^M)'}} e^{-n\beta_N U_L(\beta, \underline{\tilde{\boldsymbol{x}}}^{n=1})} \tag{2.14}$$

with n being the number of kinks of the minimum M considered in this term of the sum.

The remaining determinants of the full N-dimensional $U_N(\beta, \underline{\tilde{\boldsymbol{x}}}^M)$ surface are replaced using the results of Richardson and Althorpe [14], which are derived in the limit of large β, N and L:

$$\frac{(\det \mathbf{G}^M)'}{\det \mathbf{G}_0} = \Phi^{2n} \qquad \text{with} \qquad \Phi = \sqrt{\frac{(\det \mathbf{J}^{n=1})'}{\det \mathbf{J}_0}} \tag{2.15}$$

Similar to (2.11) the $'$ indicates that the zero frequency modes are not considered in the respective determinants. $\mathbf{G}^M$ is the Hessian of the ring polymer and $\mathbf{J}^{n=1}$ is the Hessian of the single kink minimum of the linear polymer, which is spanned between $-x_0$ and x_0. Furthermore the Hessians of the ring and linear polymer systems in which all beads are located at the bottom of one of the wells at $\pm x_0$ are referred to as $\mathbf{G}_0$ and $\mathbf{J}_0$, respectively. In the appendix of their paper Richardson and Althorpe [14] show further for the elements of $\mathbf{J}$:

$$J_{ij} = \frac{T_{ij}}{(\hbar\beta_N)^2} + V''(x_i)\delta_{ij}$$

with

$$T_{ij} = \begin{cases} 2\delta_{1j} - \delta_{1,j-1} & \text{for } i = 1 \\ 2\delta_{Lj} - \delta_{L,j+1} & \text{for } i = L \\ 2\delta_{ij} - \delta_{i,j-1} - \delta_{i,j+1} & \text{otherwise} \end{cases}$$

[3]Note that alternative definitions of the term *instanton* exist.

Evaluating the ratio of partition functions in (2.1)

Note in the limit of large β, N and L we can apply equations (2.9), (2.14) and (2.13) to result

$$\frac{\tilde{Q}_n(N_1, N_2, \ldots, N_n|\beta)}{\tilde{Q}_0(\beta)} \simeq \frac{\left(\frac{1}{\beta_N \hbar}\right)^N \left(\frac{S_{\text{kink}}}{2\pi\hbar}\right)^{n/2} \frac{(\hbar\beta_N)^n}{\sqrt{(\det \mathbf{G}^M)'}} \exp\left(-\frac{nS_{\text{kink}}}{\hbar}\right)}{\left(\frac{1}{\hbar\beta_N}\right)^2 \frac{2}{\sqrt{\det \mathbf{G}_0}}}$$
$$= \frac{1}{2}\left(\theta(\beta)\right)^n \tag{2.16}$$

where

$$\theta(\beta) = \frac{\hbar\beta_N}{\Phi}\sqrt{\frac{S_{\text{kink}}}{2\pi\hbar}} \exp\left(-\frac{S_{\text{kink}}}{\hbar}\right). \tag{2.17}$$

There are $\frac{2N^n}{n!}$ terms of this kind in (2.10), which allows us to combine (2.1) and (2.10) in this limit to yield

$$\begin{aligned}
\cosh\left(\frac{\beta\Delta}{2}\right) &= \frac{Q(\beta)}{Q_0(\beta)} \\
&\simeq \frac{\tilde{Q}(\beta)}{\tilde{Q}_0(\beta)} \\
&= 1 + \sum_{N_1,N_2} \frac{\tilde{Q}_2(N_1,N_2|\beta)}{\tilde{Q}_0(\beta)} + \sum_{N_1,N_2,N_3,N_4} \frac{\tilde{Q}_4(N_1,N_2,N_3,N_4|\beta)}{\tilde{Q}_0(\beta)} \\
&\qquad + \cdots + \sum_{N_1,N_2,\ldots,N_4} \frac{\tilde{Q}_n(N_1,N_2,\ldots,N_n|\beta)}{\tilde{Q}_0(\beta)} + \cdots \\
&= \sum_{\substack{n=0,\\ n \text{ even}}}^{\infty} \frac{2N^n}{n!} \cdot \frac{1}{2}\left(\theta(\beta)\right)^n \\
&= \cosh\left(N\theta(\beta)\right).
\end{aligned}$$

This leaves us with the final result of Richardson and Althorpe [14]

$$\Delta \simeq \frac{2}{\beta_N}\theta(\beta) \qquad \text{(large } \beta,L\text{)}$$

2.2 Generalisation to more degrees of freedom

In this section we will generalise the ideas of section 2.1 to an f-dimensional PES with two minima related by symmetry. For a system of P atoms we can choose to work in Cartesian centre of mass coordinates, which implies $f = 3P - 3$. Thence the classical Hamiltonian can be expressed as

$$H = \sum_{l=1}^{f} \frac{p_l^2}{2} + V(x_1, \ldots, x_f)$$

with x_l and p_l being the Cartesian coordinates and the momentum of the l-th degree of freedom.

Using a similar derivation to section 2.1.3 on page 5 we obtain [14]

$$Q(\beta) = \lim_{N\to\infty} \left(\frac{1}{2\pi\beta_N\hbar^2}\right)^{f\frac{N}{2}} \int_{-\infty}^{\infty} \mathrm{d}\underline{\boldsymbol{x}}\ \exp\left(-\beta_N U_N(\beta, \underline{\boldsymbol{x}})\right) \tag{2.18}$$

with

$$U_N(\beta, \underline{\boldsymbol{x}}) = \left[\sum_{i=1}^{N} V(x_{1,i}, \ldots, x_{f,i}) + \sum_{l=1}^{f} \frac{(x_{l,i+1} - x_{l,i})^2}{2\left(\beta_N\hbar\right)^2}\right]_{x_{l,N+1}=x_{l,1}}, \tag{2.19}$$

2.2.1 Interpretation of U_N and its minima

In analogy to the 1D case we can again identify U_N as an f-dimensional ring-polymer potential[4], where the N beads are f-dimensional with coordinates $x_{1,i}, x_{2,i}, \ldots, x_{f,i}$. Each of these beads is connected by f harmonic springs of frequency $\frac{1}{\hbar\beta_N}$ to its neighbours. Thereby the coordinate $x_{l,i}$ is connected to both $x_{l,i-1}$ and $x_{l,i+1}$.

Applying steepest descent to $Q(\beta)$ in analogy to 2.1.6 on page 9 requires us to determine the minima of U_N, which can again be considered as orbits on the inverted potential $-V$ [14]. Compared to above the number of these orbits, however, is drastically increased since the system as a whole is free to rotate.

[4]Note that various equivalent ideas how to interpret (2.19) as a ring-polymer potential exist. See Reid [20] for alternatives.

2.2.2 The separability of rotational motion

In a general treatment of tunnelling the splitting Δ depends on the precise rotational state of the system during tunnelling as well. In the low temperature limit (large β), however, this dependence is only very weak [14]. We can hence assume that the rotational contributions to Q are fully separable from the tunnelling dynamics and can be factored out. In the ratio $\frac{Q}{Q_0}$, in which we are mainly interested in (see (2.1)), they furthermore cancel. Overall we may hence ignore all rotations of the system as a whole and only consider the orbits of zero angular momentum. Since these orbits are distributed exactly as in the one-dimensional case the steepest descent approximation to $Q(\beta)$ is recovered as before (see (2.10) on page 11). Note, however, that we still need to consider rotations along the pathway, where — in contrast to rotations of the whole system — the beads rotate relative to one another.

2.2.3 The tunnelling splitting in higher dimensions

The remaining procedure is entirely analogous to 2.1. We describe the kinks in the ring polymer using an f-dimensional linear polymer (with L beads) connected to the minima $\pm x_{l,1}$ $(l = 1, \ldots, f)$. Its potential

$$U_L(\beta, \underline{\boldsymbol{x}}) = \sum_{i=1}^{L} V(x_{1,i}, \ldots, x_{f,i}) + \frac{1}{2(\hbar\beta_N)^2} \sum_{l=1}^{f} \left((x_{l,1} + x_{l,0})^2 + \sum_{i=1}^{L-1} (x_{l,i+1} - x_{l,i})^2 + (x_{l,0} - x_{l,L})^2 \right). \tag{2.20}$$

allows to refine the expression for S_{kink}:

$$S_{\text{kink}} = \sum_{i \in kink} \sum_{l=1}^{f} \frac{(\tilde{x}_{l,i+1} - \tilde{x}_{l,i})^2}{\hbar\beta_N}$$

In multiple dimensions the Hessian $\mathbf{J}$ of the linear has the elements [14]

$$J_{li,l'i'} = \frac{\delta_{ll'} T_{i,i'}}{(\hbar\beta_N)^2} + \delta_{ii'} \left. \frac{\partial^2 V}{\partial x_{l,i} \partial x_{l',i'}} \right|_{(x_{l,1}, \ldots, x_{f,i})} \tag{2.21}$$

with

$$T_{ii'} = \begin{cases} 2\delta_{1i'} - \delta_{1,i'-1} & \text{for } i = 1 \\ 2\delta_{Li'} - \delta_{L,i'+1} & \text{for } i = L \\ 2\delta_{ii'} - \delta_{i,i'-1} - \delta_{i,i'+1} & \text{otherwise} \end{cases}.$$

Integrating out the zero-frequency modes allows us to evaluate the ratio of partition functions $\frac{Q(\beta)}{Q_0(\beta)}$ and *summa summarum* we get the expression for the tunnelling splitting

$$\Delta \simeq \frac{2}{\beta_N}\theta(\beta) \qquad \text{(large } \beta,L), \tag{2.22}$$

where $\theta(\beta)$ is identical to (2.17) on page 14. Following our discussion in section 2.2.2 on the previous page, we also need to remove the three normal-mode frequencies associated with collective rotation of the f-dimensional linear polymer in the determinants of (2.15) to yield the correct Φ.

2.3 Tunnelling between more than two wells related by symmetry

In this section we generalise the method of the previous sections to treat tunnelling between G degenerate wells. Instead of a single splitting Δ we have a set of G distinct splittings $E_\nu - E_0$ ($\nu = 1, \ldots, G$), where E_0 is the zero-point energy of the well in the absence of tunnelling. In analogy to (2.1) we may find in the limit of large β [10]

$$\frac{Q(\beta)}{Q_0(\beta)} \simeq \frac{1}{G}\sum_{\nu=1}^{G} \exp\big(-\beta(E_\nu - E_0)\big). \tag{2.23}$$

Applying steepest descent to $Q(\beta)$ yields the equation

$$Q(\beta) = \sum_{\substack{n=0,\\ n \text{ even}}}^{\infty} \frac{N^n}{n!} \sum_{\nu=1}^{G} Q_{n,\nu}(\beta),$$

where $Q_{n,\nu}(\beta)$ represents the contributions made from all periodic orbits with n kinks that start and finish at well ν. (cf. (2.10))

We can describe the connectivity between the wells using the graph theory notation of an adjacency matrix $\mathbf{A}$. If $A_{\lambda\mu}$ gives the number of possible kinks that directly connect well λ to well μ the element $(\mathbf{A}^n)_{\nu\nu}$ gives us the number of sequences of n kinks that start and end at well ν [10].

Similar to the previous cases (see e.g. section 2.1.10 on page 12) we may factorise the tunnelling motion into the contribution of individual kinks. Denoting the action of a kink between wells λ and μ as $S_{\text{kink}}^{(\lambda\mu)}$ and the ratio of

determinants as $\Phi^{(\lambda\mu)}$ allows us to define a matrix $\mathbf{\Theta}$ with elements

$$\Theta_{\lambda\mu}(\beta) = \frac{\hbar\beta_N}{\Phi^{(\lambda\mu)}}\sqrt{\frac{S_{\text{kink}}^{(\lambda\mu)}}{2\pi\hbar}}\exp\left(-\frac{S_{\text{kink}}^{(\lambda\mu)}}{\hbar}\right) \tag{2.24}$$

(cf. equation (2.17)). Analogous to (2.16) we may write (for large β):

$$\frac{\tilde{Q}_{n,\nu}(\beta)}{\tilde{Q}_0(\beta)} \simeq \frac{1}{G}\big(\,(\mathbf{A}\circ\mathbf{\Theta})^n\,\big)_{\nu\nu}, \tag{2.25}$$

where $\circ$ denotes the elementwise matrix product

$$(\mathbf{A}\circ\mathbf{\Theta})_{\lambda\mu} = A_{\lambda\mu}\Theta_{\lambda\mu}$$

Now define the *kink path weight* matrix

$$h_{\lambda\mu} = -\lim_{\beta\to\infty}\frac{1}{\beta_N}\Theta_{\lambda\mu}(\beta). \tag{2.26}$$

and the *tunnelling matrix* $\mathbf{W} = \mathbf{A}\circ\mathbf{h}$, which enables us to recast (2.25) in the limit of large β as [10]

$$\begin{aligned}\frac{Q(\beta)}{Q_0(\beta)} &\simeq \frac{1}{G}\sum_{\substack{n=0,\\ n\text{ even}}}^{\infty}\frac{N^n}{n!}\sum_{\nu=1}^{G}\big((-\beta_N\mathbf{W})^n\big)_{\nu\nu}\\ &= \frac{1}{G}\,\mathrm{tr}\,\big(\exp(-\beta\mathbf{W})\big).\end{aligned} \tag{2.27}$$

Comparison with (2.23) shows that the desired approximations to the energy splittings $E_\nu - E_0$ are the eigenvalues of $\mathbf{W}$.

Chapter 3

Numerical implementation and computational strategies

This chapter focuses on the numerical methods required for the calculation of the tunnelling splitting. From the previous chapter we know that we need to search for the single-kink minima of the linear polymer potential — the instantons — in order to calculate the kink parameters Φ and S_{kink} in the limit of large L. In the limit of large β we can furthermore proceed to calculate $h_{\lambda\mu}$ and ultimately $\mathbf{W}$.

3.1 Finding the instantons

We use a limited memory Broyden-Fletcher-Goldfarb-Shanno (L-BFGS) algorithm [3] in order to minimise the linear polymer potential U_L of (2.20) and hence find the instanton along a given tunnelling pathway. It belongs to the class of quasi-Newton minimisation methods where the Hessian matrix is never computed explicitly. Convergence is achieved once the norm of the gradient of U_L falls below a threshold ε, which is usually chosen to be around 10^{-5} a.u..

In most calculations the terms $(x_{l,1} + x_{l,0})^2$ and $(x_{l,0} - x_{l,L})^2$ of the linear polymer potential U_L are dropped. A *loose-ended linear polymer* where the beads are no longer explicitly connected to the local minima on V, i.e. $\pm x_{l,0}$, results. In the large L limit this makes no difference for S_{kink} and Φ. It does, however, simplify the selection of an initial guess as we will see below.

Fig. 3.1 on the next page shows the stepwise convergence of a water decamer instanton, which will be considered in more depth in the next chapter. In each of the figures (a) to (h) all 256 beads of the instanton are shown simultaneously. If we name the two wells connected by the instanton A and B, the initial guess (fig. 3.1(a)) is just the linear polymer consisting of 128 beads of the local minimum in well A and 128 beads of the local minimum in well B. As the iterations progress more and more beads leave the well and fill the barrier-region in between until convergence is reached. The corresponding pathway plots, i.e. the plots of the potential V versus the distance r along the tunnelling pathway, are shown in figure 3.2 on page 22. Both figures suggest that the general shape of the instanton is established after approximately 100 iterations. Indeed in the last 400 iterations, where no real change in geometry or the pathway can be observed by eye, the gradient norm is only lowered by about $5 \cdot 10^{-5}$ a.u..

This observation turns out to be quite general: achieving the the last order of magnitude decrease in the gradient norm usually requires a disproportionate number of iterations. Especially for more expensive potentials like WHBB it might be necessary to choose a larger ε in order to make the calculation computationally affordable within acceptable time. For too large values of ε, however, the minimisation will finish too early, resulting in S_{kink} and Φ tables that show a worse or incomplete convergence (see also section 3.2 on page 23).

3.1.1 Finding an initial guess

If we use a loose-ended linear polymer as suggested above, we get a more flexible polymer system and when setting up an initial guess, rotations of the system along the pathway (cf. section 2.2.2 on page 16) do not need to be considered explicitly [14]. The disadvantage of this increased flexibility, however, is that there is no longer a constraint to which minimum of U_L we actually converge to in the minimisation. The initial guess must hence be chosen very carefully such that the resulting 1-kink minimum is actually along the right tunnelling path.

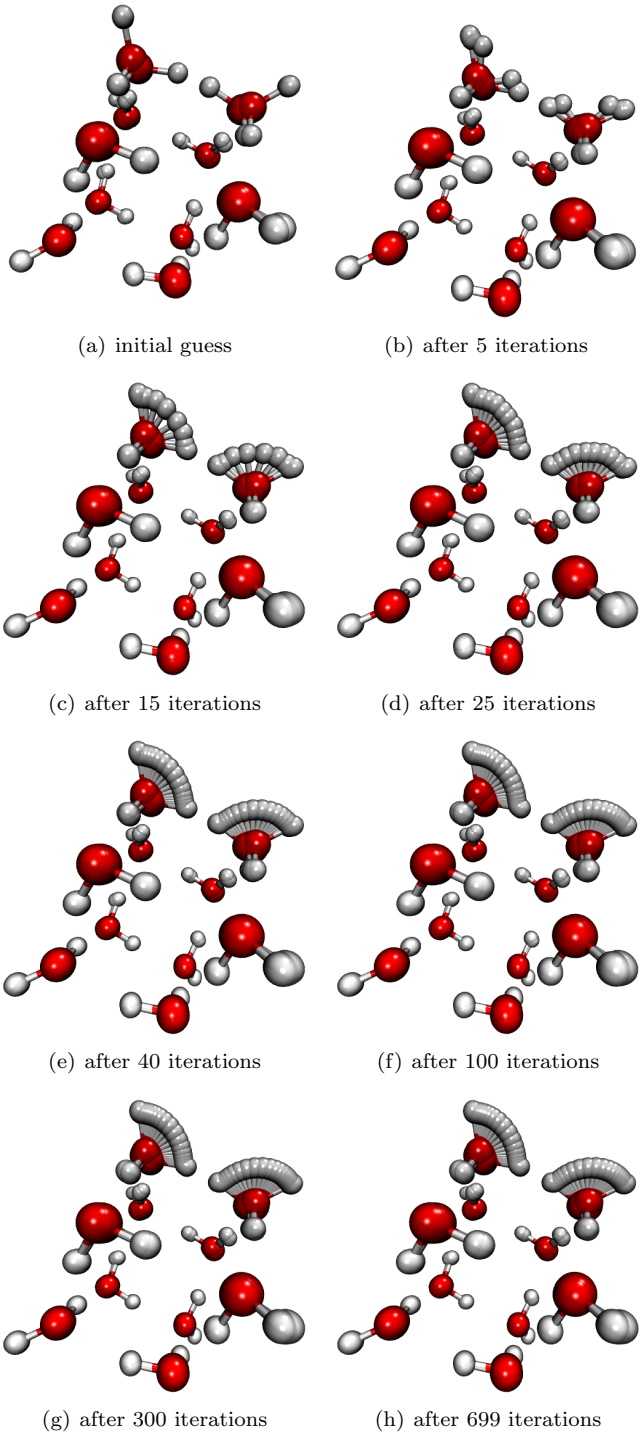

(a) initial guess (b) after 5 iterations

(c) after 15 iterations (d) after 25 iterations

(e) after 40 iterations (f) after 100 iterations

(g) after 300 iterations (h) after 699 iterations

Figure 3.1: Convergence of a water decamer instanton with 256 beads at $\hbar\beta = 20000\,\text{a.u.}$. After 699 iterations convergence to $\varepsilon = 10^{-5}\,\text{a.u.}$ was achieved.

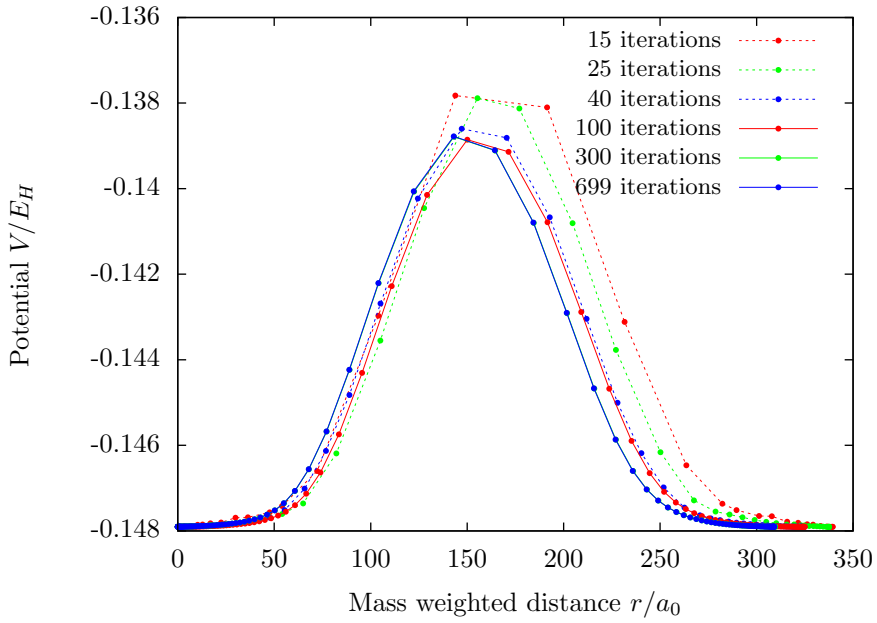

Figure 3.2: Pathway plots for the instanton guess of fig. 3.1 during minimisation with the beads depicted as bold points. Note that the plot after 300 iterations is covered by the one after 699 iterations as they are almost identical. The quantities are given in atomic units with E_H being the Hartree energy and a_0 the Bohr radius.

The most reliable method of finding an initial guess is to use an instanton of $L/2$ beads, which was already converged along the same pathway and *double the number of beads* so as to retain as much of the structure of the smaller instanton as possible. This is essentially done by adding more coordinate dimensions in the Fourier space of the bead coordinates [1].

Another option — the *setting up from scratch* — was already introduced in the example above: in this case our initial guess for an instanton connecting wells A and B would be a linear polymer consisting of $L/2$ beads which replicate the minimum geometry of well A, followed by $L/2$ beads which replicate the minimum of well B. Choosing too large a value of L results in too flexible a polymer such that the beads possibly collapse in the minimisation. If this happens all beads are located at the bottom of one well only. If we are furthermore free to choose beta we can prevent such a collapse by increasing its value. Hereby the restoring forces are reduced making it less likely for beads to be transported across the barrier.

Better than setting up from scratch is to use a converged instanton of the same L but a different β as the initial guess. Note that in the direction of increasing β, i.e. floppier springs, convergence is achieved more easily.

3.2 Obtaining the kink path weight

In order to obtain the kink path weight of a tunnelling pathway, we need to converge S_{kink} and Φ with respect to L and β. This is done by setting up tables for those quantities for various values of L and $\hbar\beta$; see for example tables 4.1 and 4.2 on page 30.

For each cell of the table the instanton with L beads spanning the considered tunnelling pathway at temperature β needs to be found. The Hessian $\mathbf{J}$ is then set up and diagonalised. Identifying and excluding the near-zero frequencies (due to rotations and the zero-frequency mode) allows us to calculate Φ. If we double the number of beads between calculations of the same $\hbar\beta$ we are able to make maximal use of the efficient doubling-beads-method for finding initial guesses. For the remaining cases of the small $N = 16$ systems we could easily set up all guesses from scratch. In practice, however, this is usually only done

[1] More precisely we set up a two-kink ring polymer (with L beads) from the old converged instanton and Fourier transform the bead coordinates. By adding L dimensions (with coordinate value zero) at the end, we keep the contributions of all normal modes, but still double the number of beads. Transforming back to real space and discarding the second kink gives the new guess.[24]

for the smallest β calculation. For the others an instanton with a smaller β is used. This allows such a table to be filled by an automated script starting from only a single human-provided guess — usually set up from scratch. See appendix A for more details on this matter.

Taking a closer look at table 4.1 we find that apart from the first row, S_{kink} is identical up to 3 significant figures along the diagonals with equal $\hbar\beta_N$ ($= \frac{\hbar\beta}{L}$). This is a sign of convergence in β [14]. For the instantons at $\hbar\beta = 10000\,\text{a.u.}$, the springs between the beads are too stiff to allow a proper sampling of the tunnelling path with beads[2]. For the remaining rows, adding more than 512 beads causes hardly any change in S_{kink}. The extra beads get mostly dumped close to the ends of the instanton (see fig. 3.3 on the following page), where they contribute only very little. The convergence of Φ (e.g. table 4.2) is usually considerably worse than S_{kink} and requires more beads to show the expected diagonal behaviour.

The best estimate for S_{kink} or Φ is given for the smallest $\hbar\beta_N$ where convergence in β has been reached — in our example this would be the cell $L = 2048$ and $\hbar\beta = 20000\,\text{a.u.}$. Although smaller values of L may already provide a good estimate for the relevant quantities [14], in this work we will use at least 1024 beads to give our estimate of S_{kink} and Φ. Those values are then used to obtain the kink path weight $h_{\lambda\mu}$ by invoking (2.26) on page 18.

[2] An equivalent idea would be to say that $\hbar\beta$ is an insufficient duration of imaginary time to connect both minima with a converged instanton.

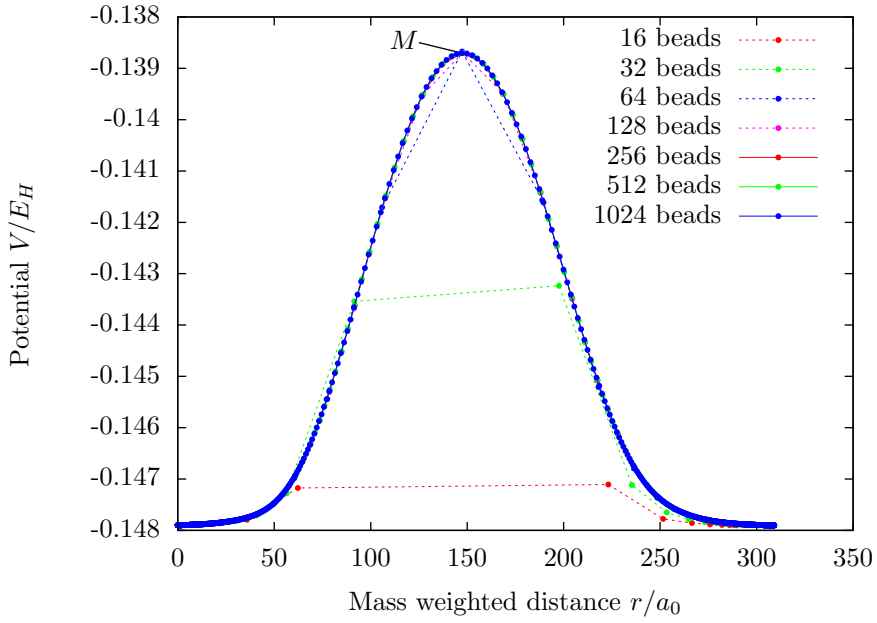

Figure 3.3: Pathway plots for the water decamer instanton at $\hbar\beta = 20000$ a.u. with various numbers of beads (bold points). The individual instantons are converged to $\varepsilon = 10^{-5}$ a.u., except in the case of 512 and 1024 beads, for which only convergence to $\varepsilon = 1.1 \cdot 10^{-5}$ a.u. was achieved. Note that, especially with 1024 beads, the majority of the beads is dumped close to the ends. The point labelled M denotes the maximum energy point reached during the pathway.

3.3 Setting up the tunnelling matrix W

For a system with more than two wells corresponding to permutation-inversion isomers, the kink path weights of tunnelling pathways which are related by symmetry are identical. Considering molecular symmetry may therefore reduce the number of elements of the matrix **W** we actually need to calculate [18]. Furthermore, tunnelling paths with an especially small $h_{\lambda\mu}$ (in magnitude) can usually be ignored (set $h_{\lambda\mu} = 0$) up to reasonable approximation. As a consequence some wells might end up not being connected to any other well in our tunnelling consideration and can be completely ignored. This reduces the dimensionality of **W**.

One basic idea to distinguish important from unimportant tunnelling pathways is to calculate rough estimates of S_{kink} and Φ (use a smaller L) and judge based on the resulting estimates of $h_{\lambda\mu}$ which pathways to investigate further. Chemical intuition, however, can also help a great deal. As $h_{\lambda\mu}$ depends strongly on S_{kink} (see (2.24) and (2.26)) and hence on the potential U_L of the instanton, anything that increases the latter will greatly reduce $h_{\lambda\mu}$. In other words tunnelling through a large tunnelling barrier is less likely. As the barrier is mainly increased by breaking bonds, only the tunnelling paths where the minimum number of hydrogen bonds are broken in the cluster contribute significantly to the splitting [18]. From the dependence of S_{kink} on the mass (via the mass-scaled coordinates $x_{l,i}$) we can also rationalise why hardly any movement of the oxygen atoms takes place in water cluster tunnelling motions.

Chapter 4

Describing tunnelling in the PP2 isomer of water decamer

Two pentagonal prism isomers of the water decamer cluster are known, which one refers to as PP1 and PP2 [25]. Here we focus only on the higher energy PP2 geometry shown in fig. 4.1. PP1, which is the decamer global minimum on the WHBB PES, deviates from the PP2 structure only slightly — the direction of the the O−H bonds forming the edges of the pentagons is reversed in the lower ring.

4.1 Labelling the PP2 isomers

Next to the atomic labels shown in fig. 4.1 we also define an *out-of-pentagon* O−H bond as one of the 10 O−H bonds which do not form part of any pentagon edge. One can easily see that each of the 10 out-of-pentagon O−H bonds can only be in one of two configurations — *up* or *down*. Due to the strong hydrogen bonding between the rings, the position of each out-of-pentagon O−H bond in the lower ring is entirely determined by the position of the out-of-pentagon bond on the oxygen atom directly above. E.g. $O_H{-}H_{16}$ can only be up since $O_C{-}H_6$ is up. Using a 5-tuple consisting of the configurations of the out-of-pentagon O−H bonds, ordered from oxygen A to E, is hence enough to distinguish 10 permutation-inversion isomers of PP2: those which are related by single flips of the out-of-pentagon O−H bonds. In the latter convention we refer to the isomer shown in fig. 4.1 as (uduud), where u stands for the O−H bond being up and d stands for it being down.

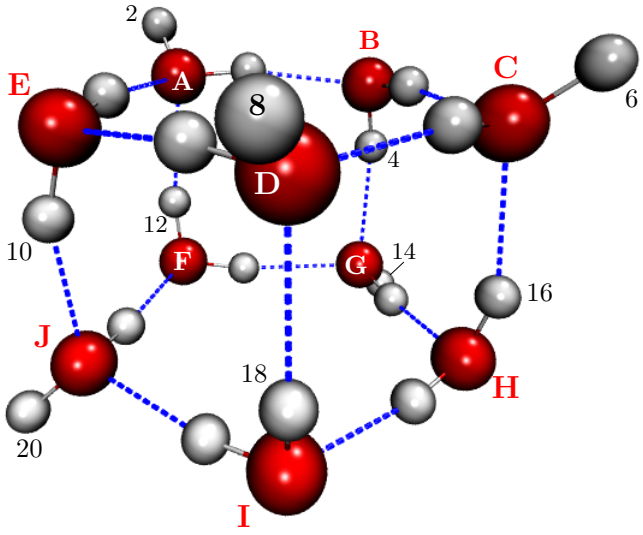

Figure 4.1: Structure of the PP2 water decamer and the definition of the labelling system used. The labels of the odd hydrogens, which are located along the edges of the pentagons, are not shown. For our labelling system H_1 is bonded to O_A, H_3 to O_B and so fourth. With respect to the position of the out-of-pentagon O−H bonds one would also label this specific isomer (uduud). See section 4.1 for more details on this.

4.2 The (uduud) ↔ (ududd) tunnelling motion

Flipping out-of-pentagon O−H bonds is also a very good candidate for a tunnelling motion. The hydrogen bond connecting the rings is the only bond that needs to be broken during tunnelling. We would therefore expect a low tunnelling barrier between the wells and hence a relatively large kink path weight as described in the previous chapter. Note, however, that only two of the five possible flips takes an isomer like (uduud) to another PP2 geometry. One of these possibilities for (uduud) is the flip of the fourth set of bonds, i.e. to yield (ududd).

The converged instanton for this motion is shown in fig. 4.2(a) as conflated snapshots of the tunnelling path. Note that this image is rotated by 72° compared to fig. 4.1 such that the oxygen O_A is now towards the LHS. Fig. 4.2(b) depicts the geometry of the maximum energy point reached during the pathway. Note that the tunnelling path does not pass through the saddle point geometry as we would expect from a transition state theory treatment. For the calculation of the instanton geometries as well as S_{kink} and Φ in tables 4.1 and 4.2 we used the WHBB potential and the procedures described in the

previous chapter with ε around 10^{-5} a.u.. The overall runtime to obtain these results was about six weeks on our hardware (see appendix B on page 50 for details). This is probably acceptable, but demonstrates the limitations of the more accurate water potentials for larger clusters. The diagonals of constant $\hbar\beta_N$ agree well for $\hbar\beta \geq 20000\,\text{a.u.}$ in both tables. According to our analysis in the previous chapter this allows us to identify the best converged values in the entry with $\hbar\beta = 20000\,\text{a.u.}$ and $L = 2048$, in other words $S_{\text{kink}} = 20.70\,\hbar$ and $\Phi = 38\,\text{a.u.}$. From (2.26) (page 18) we further find the kink path weight as $h = -1.1 \cdot 10^{-5}\,\text{cm}^{-1}$.

4.3 The tunnelling matrix and the tunnelling splittings

It is easy to see that (duddu) is the enantiomer to (uduud) and similarly (duduu) is the enantiomer to (ududd). This implies that the tunnelling pathways (uduud) $\leftrightarrow$ (ududd) and (duddu) $\leftrightarrow$ (duduu) are also enantiomerically related and must hence have the same kink path weight. A rotation of the whole latter tunnelling path by 72° such that O_A is now located at the former position of O_B yields the pathway (ududd) $\leftrightarrow$ (ududu). Once again this path has the same weight by rotational symmetry. By similar arguments one can show that all the flipping motions that convert PP2 isomers are equivalent by symmetry.

Ten wells of permutation-inversion isomers can be interconnected by such flipping motions allowing us to produce the connectivity graph shown in fig. 4.3(a) on page 31. The wells are labelled according to the system introduced in section 4.1 on page 27. Note that the kink path weight h is identical along each path (grey lines). Further tunnelling pathways surely exist — for example the tunnelling motion which permutes two hydrogen atoms within the same water molecule. Investigations of tunnelling in other large water clusters (e.g. [19] or chapter 6), however, suggest that these have much lower kink path weights and will hence not contribute much to the overall splitting.

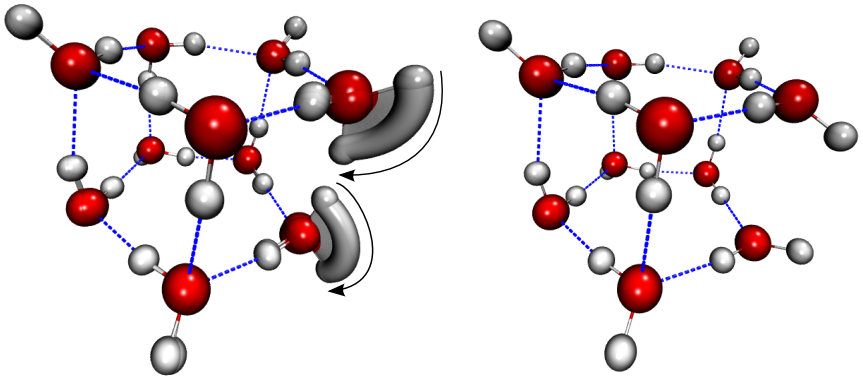

(a) Instanton (b) Tunnelling pathway energy maximum

Figure 4.2: The (uduud) ↔ (ududd) instanton: fig. (a) shows the conflated snapshots of the tunnelling path and fig. (b) the geometry of the energy maximum on the tunnelling pathway (point M in fig. 3.3).

$\hbar\beta$(a.u.) / L	16	32	64	128	256	512	1024	2048
10000	19.43	20.45	20.60	20.64	20.65	20.65	20.65	20.65
20000	12.96	19.48	20.50	20.66	20.69	20.70	20.70	20.70
40000	7.24	12.97	19.49	20.51	20.66	20.70	20.70	20.71
80000	3.89	7.24	12.97	19.49	20.51	20.66	20.70	20.70

Table 4.1: Kink actions S_{kink} of the instanton depicted in fig. 4.2(a) in reduced units of $\hbar$. The calculations were done for different numbers of linear polymer beads L and imaginary-time durations $\hbar\beta$.

$\hbar\beta$(a.u.) / L	16	32	64	128	256	512	1024	2048
10000	70	16	20	30	36	34	37	37
20000	1700	110	16	25	31	38	36	38
40000	3900	2900	250	16	23	29	37	40

Table 4.2: Determinant ratios Φ corresponding to the kink actions of table 4.1 in atomic units.

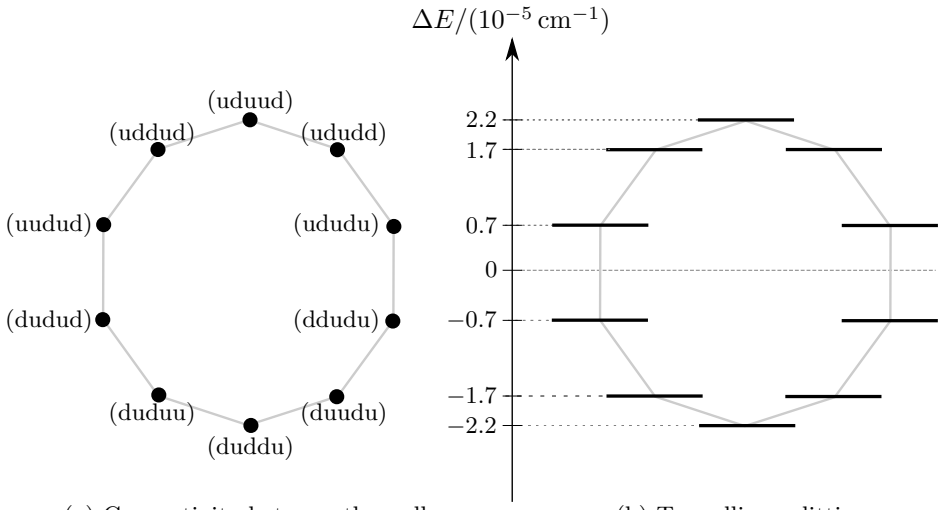

(a) Connectivity between the wells (b) Tunnelling splitting

Figure 4.3: (a) depicts the connectivity between the wells due to tunnelling, whereas (b) shows the resulting tunnelling splittings. Note the similarity in shape if the distance between the wells in (a) is chosen to represent the kink path weight. The energy scale gives the energies of the levels in (b) relative to E_0, i.e. $\Delta E = E_\nu - E_0$ and does not apply to the LHS of the figure as the wells are all degenerate.

If we only consider the 10 paths shown in figure 4.3 we obtain the following tunnelling matrix

$$\mathbf{W} = \begin{pmatrix} 0 & h & 0 & 0 & 0 & 0 & 0 & 0 & 0 & h \\ h & 0 & h & 0 & 0 & 0 & 0 & 0 & 0 & 0 \\ 0 & h & 0 & h & 0 & 0 & 0 & 0 & 0 & 0 \\ 0 & 0 & h & 0 & h & 0 & 0 & 0 & 0 & 0 \\ 0 & 0 & 0 & h & 0 & h & 0 & 0 & 0 & 0 \\ 0 & 0 & 0 & 0 & h & 0 & h & 0 & 0 & 0 \\ 0 & 0 & 0 & 0 & 0 & h & 0 & h & 0 & 0 \\ 0 & 0 & 0 & 0 & 0 & 0 & h & 0 & h & 0 \\ 0 & 0 & 0 & 0 & 0 & 0 & 0 & h & 0 & h \\ h & 0 & 0 & 0 & 0 & 0 & 0 & 0 & h & 0 \end{pmatrix}.$$

The shape of this matrix is familiar from the Hückel theory treatment of a 10 membered cyclic π system. Diagonalising $\mathbf{W}$ gives rise to the tunnelling-splitting pattern with intensity ratio 1:2:2:2:2:1 shown in fig. 4.3(b) — exactly like the energy levels in Hückel theory.

Chapter 5

Comparison of different water potentials

As shown in the previous chapter instanton calculations based on WHBB become fairly time consuming for larger systems. To go beyond the water decamer and explore tunnelling in the 19mer and 20mer (see chapter 6) a less computationally expensive alternative is required. This chapter will demonstrate that the cheaper TTM3-F potential can be used for crude estimates.

5.1 Definition and characteristics of TTM3-F and the Bowman potentials

The TTM3-F potential by Fanourgakis and Xantheas [1] is flexible, polarisable and comparatively cheap. It was parametrised to fit the vibrational spectra of water clusters as well as liquid water. The potentials HBB2 [2] and WHBB [4] — a refined successor to HBB2 — have been fitted to around 30 000 *ab initio* CCSD(T) single point calculations, which they closely reproduce. Long-range corrections were also incorporated in the latter potentials such that experimental dissociation energies are closely reproduced as well.

Whereas tunnelling splittings calculated using HBB2 gave splitting patterns in close agreement with experiment [10], it has been shown that TTM3-F possesses the wrong topology and may give rise to unrealistic stationary points along tunnelling pathways [18].

5.2 Dimer and decamer instanton calculations using the TTM3-F potential

Since the tunnelling splitting pattern is determined by the tunnelling matrix, which is in turn determined by the kink path weights h of the tunnelling instantons, it is enough to compare the values of h obtained using the different potentials in order to characterise how well the splitting patterns agree. The splitting patterns predicted using the Bowman potentials are very consistent with experimental data and hence we will assess the accuracy of the TTM3-F potential by comparing the kink path weights of Bowman and TTM3-F calculations.

As well as considering the water dimer instantons below we also used the decamer instanton depicted in fig. 4.2 on page 30 for the assessment. The calculations and convergence of S_{kink} and Φ were redone using TTM3-F as described in chapters 3 on page 19 and 4 on page 27 (see appendix C on page 51 for the convergence tables). The result is given in table 5.1 below.

5.2.1 The water dimer

Figure 5.1 depicts the water dimer structure in the TTM3-F PES and introduces the labelling system. A common convention to describe the dimer instantons is to use permutations of the oxygen and hydrogen labels. The permutation (12) for example is assigned to a tunnelling motion which swaps hydrogen atoms 1 and 2. The five instantons we reconsidered here with the TTM3-F potential are the ones which Richardson et al. [10] found to give rise to the observed dimer splitting. Following the usual procedure and using a gradient threshold $\varepsilon = 10^{-5}$ a.u. produces tables in S_{kink} and Φ which show — apart from the first row where the springs are too stiff in some of the instantons — a good diagonal pattern (see appendix C for details). The converged instanton tunnelling paths are depicted in fig. 5.2.

5.2.2 Comparison to the results obtained with Bowman potentials

The converged results of the instanton calculations outlined above are summarised in table 5.1 on page 35 next to the equivalent results if Bowman potentials are used (see chapter 4 and [10]). In the dimer — apart from the bifurcation tunnelling pathway — the kink path weights agree up to a factor of 2. Considering the columns of Φ and S_{kink}, however, we note that this seems

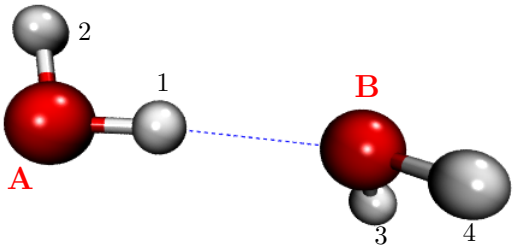

Figure 5.1: Structure of the water dimer. The labels are used to identify the motion along a tunnelling pathway. The permutation (12), for example, denotes that the tunnelling motion which involves swapping hydrogens 1 and 2.

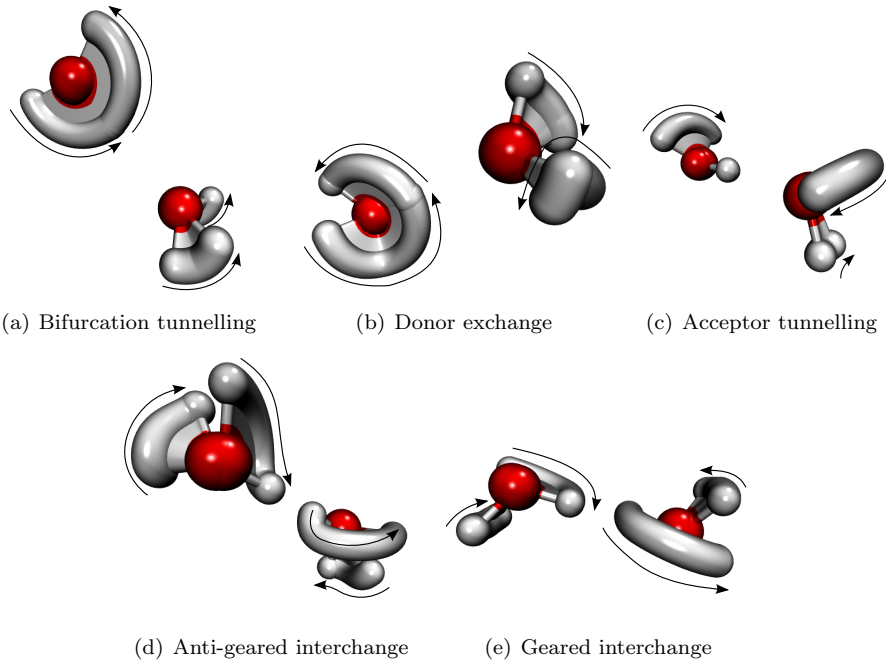

(a) Bifurcation tunnelling (b) Donor exchange (c) Acceptor tunnelling

(d) Anti-geared interchange (e) Geared interchange

Figure 5.2: Conflated snapshots of the dimer instanton tunneling paths obtained using the TTM3-F potential.

Cluster	Pathway	Permutation	potential	$S_{\text{kink}}/\hbar$	Φ/(a.u.)	$-h/\text{cm}^{-1}$
10mer	see fig. 4.2 on page 30		WHBB	20.70	38	$1.1 \cdot 10^{-5}$
			TTM3-F	20.47	330	$1.6 \cdot 10^{-6}$
2mer	Bifurcation tunnelling	(12)(34)	HBB2	12.04	51	0.035
			TTM3-F	12.58	130	0.0079
2mer	Donor exchange	(12)	HBB2	15.94	18	0.0023
			TTM3-F	15.56	32	0.0018
2mer	Acceptor tunnelling	(34)	HBB2	5.74	120	5.5
			TTM3-F	3.32	540	11
2mer	Anti-geared interchange	(AB)(14)(23)	HBB2	11.17	140	0.029
			TTM3-F	10.41	230	0.037
2mer	Geared interchange	(AB)(1324)	HBB2	7.48	720	0.19
			TTM3-F	6.87	1600	0.15

Table 5.1: Comparison of results from instanton calculations using the TTM3-F and Bowman potentials. Permutations are given with respect to the labels in fig. 5.1. Illustrations of the dimer instantons are given in fig. 5.2. The numbers for all dimer HBB2 calculations were taken from [10].

to be accidental for some cases. Nevertheless for all the instantons considered the maximum deviation of S_{kink}, Φ and h was an order of magnitude. A similar agreement of these quantities has also been demonstrated for the water trimer instantons [10]. Overall we therefore expect that for even larger systems the TTM3-F potential allows us to distinguish between instantons which make a significant contribution to the tunnelling matrix and those that can be ignored.

Note that the dimer bifurcation tunnelling motion is one of the cases where the TTM3-F potential possesses an unrealistic extra local minimum on the pathway. This explains the large deviation by a factor of about 20.

Comparing the computational times necessary to set up the S_{kink} and Φ tables for one instanton, the difference is only marginal for the dimer — three hours using TTM3-F vs. four hours with WHBB. For the decamer, however, the six weeks of walltime using WHBB reduce to only two days using TTM3-F! Although in small systems the increased accuracy obtained using the Bowman PES outweighs the saved computational time, for larger systems seeking tunnelling paths can be greatly sped up using TTM3-F. From the rough estimates of the kink path weights obtained with the TTM3-F potential we can select the promising tunnelling pathways — i.e. the giving large values of h — and further investigate them using more accurate potentials.

Chapter 6

TTM3-F instanton calculations on larger systems

In this chapter we will perform instanton calculations on the water enneakaidecamer (19mer) and icosamer (20mer). For both clusters two instantons are studied using the TTM3-F potential.

Although RPI theory is only derived for cases of *degenerate tunnelling*, i.e. the cases where tunnelling takes place between degenerate wells, the case of *non-degenerate tunnelling* is also possible. Similar to a bad energy match in MO theory the interaction of the ground states Ψ_L and Ψ_R (cf. section 2.1.1 on page 4) is very weak in non-degenerate tunnelling between two wells. The resulting tunnelling splitting is therefore extremely small. For our treatment of the 19mer and 20mer in this chapter we will completely ignore the possibility of non-degenerate tunnelling.

6.1 The icosamer (20mer)

The water 20mer has the structure of two layers of three fused pentagons stacked on top of each other (see fig. 6.1). This is a very rigid system meaning that each water molecule participates in at least three hydrogen bonds. A flipping tunnelling motion such as we considered in the water decamer (cf. fig. 4.2(a)) is very improbable since almost all hydrogen bonds would need to rearrange (for degenerate tunnelling). The only water molecules which are reasonably free to move are the 12 molecules sitting in the three squares furthest away from the

centre. Again due to the rigidity of the cluster we can only imagine a rotation of one of these molecules by 180° as a tunnelling pathway — i.e. effectively a permutation of the hydrogen labels of one H_2O molecule. Two such pathways are shown in fig. 6.2: an acceptor-acceptor-donor (AAD) instanton in fig. 6.2(a) and a donor-donor-acceptor (DDA) instanton in fig. 6.2(b). Note that the classification refers to the type of water molecule rotating.

We set up the S_{kink} and Φ tables for these pathways (see tables 6.1 and 6.2) following the method of chapter 3 on page 19. Although the instantons are not fully converged yet, which is evident from the behaviour of the Φ values, we are still able to obtain ballpark figures for the expected kink path weights. Assuming that the cell with $\hbar\beta = 20000$, $L = 1024$ contains the most converged value we find for the AAD instanton $S_{\text{kink}} = 29.22\,\hbar$, $\Phi = 350\,\text{a.u.}$ and $h = -2.63 \cdot 10^{-10}\,\text{cm}^{-1}$. For the DDA instanton, however, we obtain $S_{\text{kink}} = 33.68\,\hbar$, $\Phi = 58\,\text{a.u.}$ and $h = -2.06 \cdot 10^{-11}\,\text{cm}^{-1}$. The differences in the respective S_{kink} and h values can be easily rationalised from the fact that in the tunnelling motion of the DDA instanton we need to break 2 hydrogen bonds and in the motion of the AAD instanton only one. Therefore the former has a higher tunnelling barrier.

Compared to the values of the kink path weights we calculated in the previous chapters the ones obtained here are very small. In fact the splittings they would give rise to are too small to be observed [19] and hence these pathways can be ignored in a splitting calculation. Taking another look at fig. 6.2 we note very little movement in the 20mer apart from the tunnelling hydrogens. Hence the exact site of rotation is almost irrelevant and any other rotation involving one of the 10 remaining less constrained water molecules would give rise to kink path weights which are of a similar order of magnitude. Although only TTM3-F calculations were carried out and those were furthermore not fully converged we may still conclude that tunnelling effects are highly unlikely to play a role in the VRT spectrum of water 20mer.

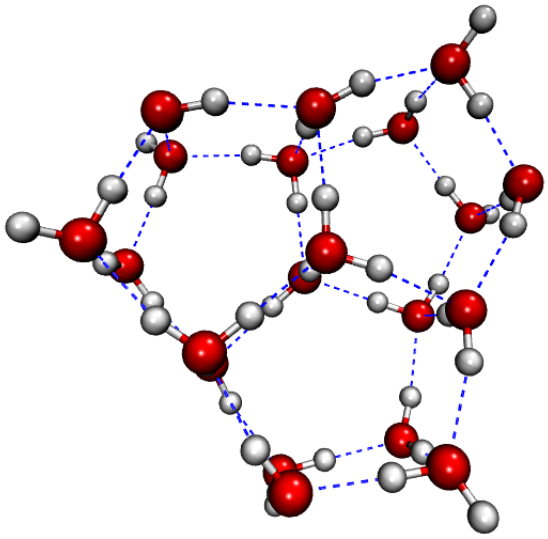

Figure 6.1: Structure of the icosamer (20mer)

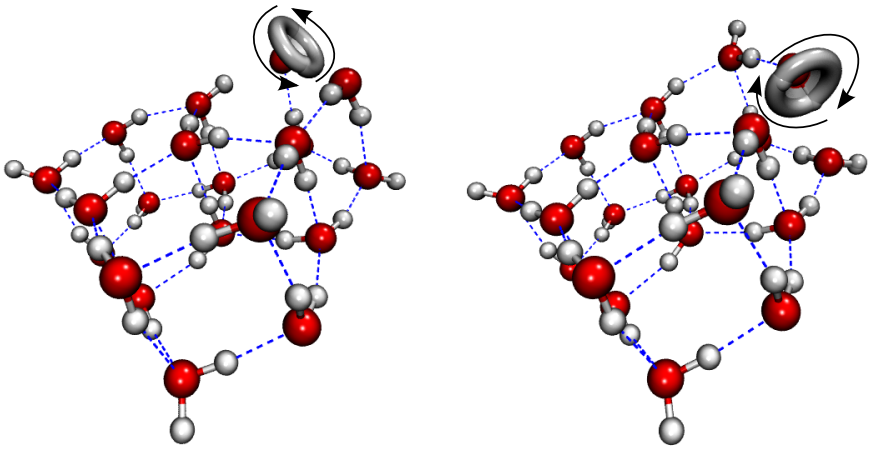

(a) AAD instanton (b) DDA instanton

Figure 6.2: Conflated snapshots of the considered 20mer tunnelling paths. The structures were obtained using the TTM3-F potential.

	AAD instanton (fig. 6.2(a))						
$\hbar\beta$(a.u.) / L	16	32	64	128	256	512	1024
10000	24.75	28.75	29.09	29.17	29.19	29.19	29.19
20000	12.80	24.74	28.78	29.11	29.19	29.21	29.22
40000	6.46	12.80	24.74	28.78	29.12	29.20	29.22
80000		6.46	12.80	24.74	28.78	29.12	29.20

	DDA instanton (fig. 6.2(b))						
$\hbar\beta$(a.u.) / L	16	32	64	128	256	512	1024
10000	24.46	33.06	33.51	33.61	33.64	33.64	33.64
20000	12.62	24.46	33.09	33.55	33.65	33.68	33.68
40000	6.36	12.62	24.46	33.10	33.55	33.66	33.68
80000		6.36	12.62	24.46	33.10	33.55	33.66

Table 6.1: Kink actions S_{kink} of the 20mer AAD instanton depicted in fig. 6.2 in reduced units of $\hbar$. The calculations were done using the TTM3-F PES for different numbers of linear polymer beads L and imaginary-time durations $\hbar\beta$ with a gradient threshold $\varepsilon = 10^{-4}$ a.u. as described in chapter 3 on page 19.

	AAD instanton (fig. 6.2(a))						
$\hbar\beta$(a.u.) / L	16	32	64	128	256	512	1024
10000	240	99	160	230	290	310	320
20000	2300	330	88	170	270	330	350
40000	9000	13000	7.60	97	180	290	360

	DDA instanton (fig. 6.2(b))						
$\hbar\beta$(a.u.) / L	16	32	64	128	256	512	1024
10000	1000	13	23	39	52	57	58
20000	3200	1600	14	24	41	54	58
40000	10000	8800	3300	16	27	47	62
80000		22000	20000	8900	15	28	51

Table 6.2: Determinant ratios Φ corresponding to the kink actions of table 6.1 in atomic units.

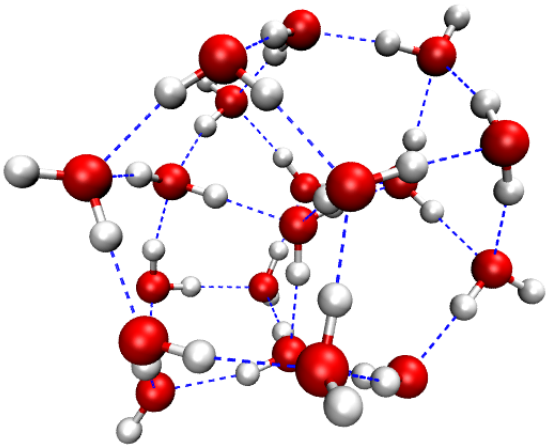

Figure 6.3: Structure of the enneakaidecamer (19mer)

6.2 The enneakaidecamer (19mer)

The 19mer is only considered briefly here. Although the structure of this cluster is less regular (see fig. 6.3), the tunnelling situation is only marginally different: it is also rigid and does not allow hydrogen flips. In a similar fashion to the 20mer we briefly considered an AAD-type and a DDA-type instanton. Their TTM3-F geometries are shown in fig. 6.4. From table 6.3 we estimate S_{kink} as $27.44\,\hbar$ for the ADD and $33.33\,\hbar$ for the DDA instanton. The Φ tables did not converge to any specific value and were therefore left out. An order of magnitude estimate of h was nevertheless possible and gave values of the order of $10^{-8}\,\text{cm}^{-1}$ to $10^{-9}\,\text{cm}^{-1}$ for both instantons. Once again this is too small to yield an experimentally observable feature. A similar chain of arguments to that above leads to the conclusion that tunnelling effects are negligible in the the VRT spectrum of this cluster as well.

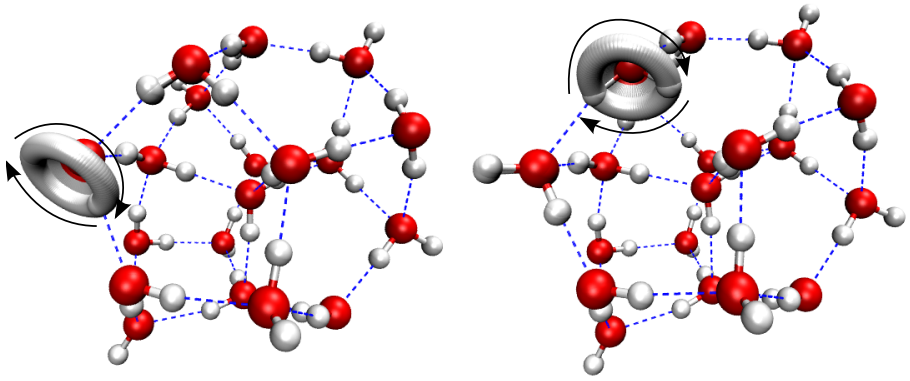

(a) AAD instanton (b) DDA instanton

Figure 6.4: Conflated snapshots of the 19mer tunnelling paths considered. The TTM3-F potential was used to obtain these structures.

	AAD instanton (fig. 6.4(a))					
$\hbar\beta$(a.u.) / L	32	64	128	256	512	1024
10000	27.06	27.33	27.39	27.40	27.41	27.41
20000	24.45	27.09	27.36	27.42	27.43	27.44
40000	12.78	24.45	27.09	27.36	27.42	27.44
80000	6.45	12.78	24.45	27.09	27.36	27.42

	DDA instanton (fig. 6.4(b))					
$\hbar\beta$(a.u.) / L	32	64	128	256	512	1024
10000	32.68	33.13	33.23	33.25	33.26	33.26
20000	24.20	32.74	33.19	33.30	33.32	33.33
40000	12.48	24.20	32.75	33.20	33.30	33.33
80000	6.29	12.48	24.20	32.75	33.20	33.30
160000		6.29	12.48	24.20	32.75	33.20

Table 6.3: Kink actions S_{kink} of the 19mer instantons depicted in fig. 6.4 in reduced units of $\hbar$. All calculations were done using the TTM3-F potential and with a gradient threshold of $\varepsilon = 10^{-4}$ a.u..

Chapter 7

Conclusions

Using the accurate WHBB potential we were able to make realistic predictions of the splittings of spectral lines in the vibration-rotation-tunnelling spectrum of the PP2 isomer of water decamer. Due to the symmetry of this cluster we achieved this with a single instanton calculation, which gave a kink path weight of $h = -1.1 \cdot 10^{-5}\,\mathrm{cm}^{-1}$ — an experimentally observable quantity. The circular arrangement of the wells connected by tunnelling lead to a 10-dimensional Hückel-like tunnelling matrix **W** and lead to the splitting pattern of fig. 4.3 on page 31 with intensity ratios 1:2:2:2:2:1.

Next we compared the cheaper, but less accurate TTM3-F to the Bowman potentials WHBB and HBB2 using the dimer and PP2-decamer instantons as test cases. This investigation showed that the results of the TTM3-F calculations were never out by more than an order of magnitude although the calculations proceeded a lot faster for larger systems like the decamer. Using such a computationally cheaper potential hence provides a good first guess for the kink path weight and allows us to identify tunnelling paths that can be ignored in the matrix **W**.

Finally we explored two examples of instantons in both the water enneakaidecamer (19mer) and the icosamer (20mer). Although only the TTM3-F potential was used the small kink paths we obtained and the relative rigidity of both these clusters led to the conclusion that the tunnelling splittings in these clusters will most likely be too small to be observed.

Larger water clusters approach a more "spherical" form in which the number of hydrogen bonds is maximised (consider for example the 19mer in fig. 6.3). As a result the O−H bonds are overall less flexible, requiring the tunnelling barrier to be larger. This means that tunnelling motions involving configurational changes, such as the "drop"-like decamer instanton of fig. 4.2(a) on page 30, become very unlikely in those clusters. Tunnelling motions, however, in which no configurational changes take place, seem to have small kink path weights, cf. the 19mer, 20mer or the octamer [19] instantons. In summary this suggests that only water clusters that are not of a "spherical" shape will show an experimentally observable splitting. Such shapes, however, become the exception rather than the rule for larger clusters.

Chapter 8

Ideas for further work

The methods discussed here can easily be applied to other large water clusters as well. With the TTM3-F potential guesses for kink path weights are cheap and give a rough idea of the size of the splitting. As indicated above our findings suggest that only a few of the larger clusters have observable tunnelling splittings. Using TTM3-F calculations in order to screen a wide range of large clusters allows us to investigate this further by easily identifying those clusters which only show unobservable splittings.

One of the most difficult steps when trying to calculate the tunnelling splittings is to find the initial guess for the tunnelling pathway; i.e. to visualise the molecule and spot places where a tunnelling motion could occur. This becomes especially hard for larger systems like the 19mer and 20mer. A remedy for this could be an automatic search algorithm for instanton guesses. By parsing the cluster structure for known patterns in the water arrangement that give rise to tunnelling paths, we could identify potential tunnelling sites. Determining the number of hydrogen bonds broken in the tunnelling motion and TTM3-F calculations of the relative kink path weights would then validate these guesses. Promising tunnelling paths could then be presented to the user, who could proceed to more accurate calculations using e.g. the Bowman potentials.

In principle the RPI method could also be improved if the stationary beads that accumulate at the bottom of the wells (see fig. 3.3 on page 25) could be factored out and removed from the calculation. A reduction of the dimensionality of the minimisation would be the result. This problem is subject to ongoing research at the moment.

Appendix A

Scripts written to ease computation and analysis

This appendix gives excerpts from a few of the scripts I wrote in order to automate the convergence of the initial guesses as well as the calculation of the S_{kink} and Φ tables.

A.1 Convergence of initial guesses

This script sets up an initial guess from scratch taking guesses or exact geometries of the minima of the two wells connected by the tunnelling pathway.

```
#!/bin/bash
#
# Definition of a few variables
# ...

optbead() {
  #Optimise a single bead
  #$1: file with guess
  #$2: folder to create and carry out optimisation
  #$3: shall we write data: 1 for yes

  echo "###################################"
  echo "#-- Optimising bead $1"
  echo "###################################"
  echo

  #EPS is the epsilon value we want to converge the instanton to
  #the beads at start and end need to be converged tighter, hence
  #devide by 100
  #PES gives the potential to be used
```

```
  local OEPS=`echo "$EPS" | awk '{printf "%G", $1/100}'`
  local ARGS=" --maxiter $MAXITER --pes $PES --eps $OEPS guess.xyz"
  if [ "$3" = "1" ]; then
    ARGS="--writedata $DATA $ARGS"
  else
    #we just need the geometry
    ARGS="--nohess $ARGS"
  fi

  mkdir -p "$2"
  cp $1 "$2/guess.xyz"
  # go into subshell:
  (
    cd "$2"
    #linpolexe is the program to do the minimisation and
    #calculation of the splitting parameters
    eval "linpolexe $ARGS"

    if [ "$?" != "0" ]; then
      echo "Linpolexe returned with an error"
        exit 1
    fi
  )
  [ "$?" != "0" ] && exit 1
  echo
  echo
}

build_instantion() {
  #build the initial guess made out of bead duplicates of
  #the structure in the first well and the second well
  #N is the number of beads we want for the initial guess
  NSTARTEND=$((N/2))

  mkdir -p "$INSTANTFOLDER"

  cp "$START" "$INSTANTFOLDER/start.xyz"
  cp "$END" "$INSTANTFOLDER/end.xyz"

  rm -f "$INSTANTFOLDER/instanton_guess.xyz"


  #add starting geometry at the beginning:
  for (( i=1; i <= $NSTARTEND; i++)); do
    cat "$INSTANTFOLDER/start.xyz" >> \
      "$INSTANTFOLDER/instanton_guess.xyz"
  done

  #add end geometry at the end:
  for ((i=$NSTARTEND+1;i <= $N;i++)); do
```

```
71      cat "$INSTANTFOLDER/end.xyz" >> \
          "$INSTANTFOLDER/instanton_guess.xyz"
    done

    #0change_beta.sh changes the beta value of an instanton xyz file
76  0change_beta.sh "$INSTANTFOLDER/instanton_guess.xyz" "$BETA"
  }

  opt_instanton() {
    #$1: Folder
81  #$2: EPS to use
    #$3: Extra Args

    echo "###################################"
    echo "#-- Optimising instanton $1"
86  echo "###################################"
    echo

    #go to subshell:
    (
91    cd "$1"
      #mpigo runs the linpolexe program using NPROC processors in
          parallel
      #if the execution terminates the user $TO getsinformed via mail
      mpigo.sh -t $TO -p $NPROC -x linpolexe -- --maxiter $MAXITER \
        --pes $PES --eps $2 --data "$DATA" $3 input.xyz
96    if [ "$?" != "0" ]; then
        echo "Linpolexe returned with an error"
          exit 1
      fi

101   #check if the calculation has finished successfully and is sane
      0check_Linpol_Calculation.sh .
      if [ "$?" != "0" ]; then
        echo "Linpolexe Calculation result check failed"
          exit 1
106   fi
    )
    [ "$?" != "0" ] && exit 1
    echo
    echo
111 }

  while [ "$1" ]; do
    #read command line arguments and take action

116 done
  #-----------------------------------------

  #checks the input and displays a summary of what is done
```

```
check_configuration
display_summary

#if user wishes optimise the guess for first well minimum
if [ "$OPTEND" -eq "1" ];then
  optbead "$END" "$ENDFOLDER" $ENDWRITEDATA
  END=`echo $ENDFOLDER/????????-??????-optimi?ed.xyz`
fi

#if user wishes optimise the guess for second well minimum
if [ "$OPTSTART" -eq "1" ];then
  optbead "$START" "$STARTFOLDER" $STARTWRITEDATA
  START=`echo $STARTFOLDER/????????-??????-optimi?ed.xyz`
fi

build_instantion

cd "$INSTANTFOLDER"
PREV="instanton_guess.xyz"

mkdir -p "$EPS"
cp "$PREV" "$EPS/input.xyz"
opt_instanton "$EPS" "$EPS"

exit 0
```

A.2 Setting up convergence tables

The script system to set up the convergence tables consists of two scripts. The first script takes the initial guess computed above, initialises the directory structure and writes the second script. The latter is then used to execute the calculations in the manner described in chapter 3 on page 19. The calculation behind a cell in the S_{kink} or Φ tables is done in the subdirectory $\hbar\beta/L$ — i.e. the rows are the first level of the directory structure which have the bead numbers L as subdirectories. See below a snippet of the second script, which deals with the precise execution of the `linpolexe` program used to do the linear polymer calculations and converge a single instanton. The snippet given below does the calculation for $\hbar\beta = 20000\,\text{a.u.}$, $L = 32$.

```
cd 20000/32
#read the config file with the name of the INPUT file
#and the minimisation parameter EPS used
#and stores the results to LINPOL_ARGS
read_config

echo "Invoke mpigo for 20000/32" >> $LOG
echo -n "Calculating (20000,32)  "
```

```
#run linpolexe using 16 processors and save output to a logfile
mpigo.sh -t $CHILDTO -p 16 -x "$LINPOLEXE" -- --pes \
  $PES $LINPOL_ARGS  &>> $LOG

if [ "$?" != "0" ]; then
  echo "...  ERROR"
  echo "Error running mpigo.sh -x \"$LINPOLEXE\"" >> $LOG
  echo "Aborting" >> $LOG
  #error occurred => inform user and send him log via mail
  send_log "20000/32: mpigo/linpolexe failed"
  exit 1
fi
echo "...  done"

echo "Checking results for 20000/32" >> $LOG
0check_Linpol_Calculation.sh . >> $LOG
if [ "$?" != "0" ]; then
  echo "Calculation not ok!" >> $LOG
  echo "Aborting" >> $LOG
  send_log "20000/32: results check failed"
  exit 1
fi

#double the number of beads and store in folder 20000/64
OPT=`ls -1t ????????-??????-optimized.xyz | head -n1`
0double.sh "$OPT" "../64/input.xyz"
if [ "$?" != "0" ]; then
  echo "Error doubling beads from 32 to 64" >> $LOG
  echo "Aborting" >> $LOG
  send_log "20000/32: error doubling beads"
  exit 1
fi

#copy the geometry to the equivalent calculation with larger BETA
cp "$OPT" "../../40000/32/input.xyz"
if [ "$?" != "0" ]; then
  echo "Error copying bead geometry from 20000/32 to 40000/32" \
    >> $LOG
  echo "Aborting" >> $LOG
  send_log "20000/32: error copying bead geometry"
  exit 1
fi
0change_beta.sh "../../40000/32/input.xyz" "40000"
echo "20000/32 (opt. geometry)" > "../../40000/32/input_from"
```

Appendix B

Computational Information

Hardware All calculations were done on a single computer with a 16-core Intel Xeon E5540 CPU operating at 2.53GHz and 15.6GiB RAM.

Software The minimisation of the linear polymers to instantons and the subsequent calculation of the parameters S_{kink}, Φ and h is done using the program `linpolexe`. It has been developed recently in the Althorpe group by

- Adam A. Reid — concept and contribution of most of the code, including parallelisation of the minimisation.
- Michael F. Herbst — structural enhancements, parallelisation of the Hessian calculation, calculation of Φ and h.
- Marko Cvitas — adaption of the L-BFGS algorithm.
- Jeremy O. Richardson — algorithmic improvements.

Overall the minimisation and the calculation of the Hessian matrix is fully parallelised using Open MPI and scales well. The diagonalisation of the Hessian, however, is still done using a single core only.

Compilation The code was compiled using `ifort` 13.0.0 with the flags `-O2 -ip -ipo -axSSE4.2` and linked to the Intel MKL library for LAPACK support.

Runtime Calculation of the water decamer convergence tables (cf. tables 4.1 and 4.2) took six weeks when the WHBB potential was used and two days for TTM3-F.

Appendix C

Further TTM3-F convergence tables

This appendix presents the raw convergence tables for the decamer and dimer instanton calculations using the TTM3-F potential. As usual L denotes the number of linear polymer beads and $\hbar\beta$ the imaginary-time durations used for the calculation in the respective cells. S_{kink} is given in units of $\hbar$ and Φ is given in atomic units.

C.1 Decamer instanton of fig. 4.2

	$S_{\text{kink}}/\hbar$							
$\hbar\beta$(a.u.) / L	16	32	64	128	256	512	1024	2048
20000	13.66	19.20	20.28	20.42	20.45	20.46	20.46	20.46
40000	8.37	13.67	19.21	20.29	20.43	20.46	20.47	20.47
80000		8.37	13.67	19.21	20.29	20.43	20.46	20.47

	Φ/(a.u.)							
$\hbar\beta$(a.u.) / L	16	32	64	128	256	512	1024	2048
20000	2900	910	170	190	300	380	420	420
40000	8400	7400	1200	140	150	250	300	330
80000		15000	15000	2200	150	150	250	288

C.2 Bifurcation tunnelling, permutation (12)(34)

This and the remaining sections deal with dimer instantons.

	$S_{\mathrm{kink}}/\hbar$							
$\hbar\beta$(a.u.) / L	32	64	128	256	512	1024	2048	4096
20000	12.37	12.53	12.57	12.58	12.58	12.58	12.58	12.58
40000	10.67	12.37	12.53	12.57	12.58	12.58	12.58	12.58
80000	6.73	10.67	12.36	12.53	12.57	12.58	12.58	12.58

	Φ/(a.u.)							
$\hbar\beta$(a.u.) / L	32	64	128	256	512	1024	2048	4096
20000	69	73	93	120	130	140	140	140
40000	810	68	72	91	110	130	130	130
80000	3000	1500	200	71	90	110	130	130

C.3 Donor exchange, permutation (12)

	$S_{\mathrm{kink}}/\hbar$						
$\hbar\beta$(a.u.) / L	32	64	128	256	512	1024	2048
40000	12.07	15.31	15.50	15.55	15.56	15.56	15.56
80000	6.11	12.07	15.31	15.50	15.55	15.56	15.56

	Φ/(a.u.)						
$\hbar\beta$(a.u.) / L	32	64	128	256	512	1024	2048
40000	1200	23	15	21	27	31	32
80000	6300	2000	41	15	20	26	31

C.4 Acceptor tunnelling, permutation (34)

	$S_{\mathrm{kink}}/\hbar$							
$\hbar\beta$(a.u.) / L	32	64	128	256	512	1024	2048	4096
20000	3.31	3.31	3.32	3.32	3.32	3.32	3.32	3.32
40000	3.30	3.31	3.32	3.32	3.32	3.32	3.32	3.32
80000	3.23	3.30	3.31	3.32	3.32	3.32	3.32	3.32

	Φ/(a.u.)							
$\hbar\beta$(a.u.) / L	32	64	128	256	512	1024	2048	4096
20000	440	450	480	510	530	530	540	540
40000	440	430	440	470	510	520	530	530
80000	490	430	420	430	460	500	510	520

C.5 Anti-geared interchange, permutation (AB)(14)(23)

	$S_{\mathrm{kink}}/\hbar$							
$\hbar\beta$(a.u.) / L	32	64	128	256	512	1024	2048	4096
20000	10.35	10.40	10.40	10.41	10.41	10.41	10.41	10.41
40000	10.16	10.36	10.40	10.41	10.41	10.41	10.41	10.41
80000	9.23	10.16	10.36	10.40	10.41	10.41	10.41	10.41

	Φ/(a.u.)							
$\hbar\beta$(a.u.) / L	32	64	128	256	512	1024	2048	4096
20000	220	270	240	240	230	230	230	230
40000	270	210	230	220	230	230	240	230
80000	1100	530	220	220	210	210	220	230

C.6 Geared interchange, permutation (AB)(1324)

	$S_{\mathrm{kink}}/\hbar$							
$\hbar\beta$(a.u.) / L	32	64	128	256	512	1024	2048	4096
20000	6.85	6.87	6.87	6.87	6.87	6.87	6.87	6.87
40000	6.77	6.85	6.87	6.87	6.87	6.87	6.87	6.87
80000	6.50	6.78	6.85	6.87	6.87	6.87	6.87	6.87

	Φ/(a.u.)							
$\hbar\beta$(a.u.) / L	32	64	128	256	512	1024	2048	4096
20000	2000	2700	2200	1800	1600	1600	1600	1600
40000	2300	2000	2000	1700	1600	1500	1600	1600
80000	36000	1500	2000	1900	1900	1700	1800	1500

Bibliography

[1] George S. Fanourgakis and Sotiris S. Xantheas. Development of transferable interaction potentials for water. V. Extension of the flexible, polarizable, Thole-type model potential (TTM3-F, v. 3.0) to describe the vibrational spectra of water clusters and liquid water. *J. Chem. Phys.*, 128(7):074506, 2008. doi: 10.1063/1.2837299. URL `http://link.aip.org/link/?JCP/128/074506/1`.

[2] Yimin Wang, Benjamin C. Shepler, Bastiaan J. Braams, and Joel M. Bowman. Full-dimensional, ab initio potential energy and dipole moment surfaces for water. *J. Chem. Phys.*, 131(5):054511, 2009. doi: 10.1063/1.3196178. URL `http://link.aip.org/link/?JCP/131/054511/1`.

[3] Jorge Nocedal. Updating quasi-newton matrices with limited storage. *Math. Comp.*, 35(151):773–782, 1980. ISSN 0025-5718. doi: 10.2307/2006193.

[4] Yimin Wang and Joel M. Bowman. Ab initio potential and dipole moment surfaces for water. II. Local-monomer calculations of the infrared spectra of water clusters. *J. Chem. Phys.*, 134(15):154510, 2011. doi: 10.1063/1.3579995. URL `http://link.aip.org/link/?JCP/134/154510/1`.

[5] Günter Nimtz and Astrid Haibel. *Zero time space : How quantum tunneling broke the light speed barrier*. Wiley-VCH, Weinheim, 2008. ISBN 9783527407354 (pbk.).

[6] Friedrich Hund. Zur Deutung der Molekelspektren. I. *Z. Angew. Phys.*, 40:742–764, 1927. ISSN 0044-3328. doi: 10.1007/BF01400234. URL `http://dx.doi.org/10.1007/BF01400234`.

[7] Claud E. Cleeton and Nicholas H. Williams. Electromagnetic waves of 1.1 cm wave-length and the absorption spectrum of ammonia. *Phys. Rev.*, 45:234–237, Feb 1934. doi: 10.1103/PhysRev.45.234. URL `http://link.aps.org/doi/10.1103/PhysRev.45.234`.

[8] Philip R Bunker and Per Jensen. *Fundamentals of molecular symmetry*. Institute of Physics Pub, Bristol, 2005. ISBN 0750309415 (pbk.).

[9] Frank N. Keutsch and Richard J. Saykally. Water clusters: Untangling the mysteries of the liquid, one molecule at a time. *Proc. Natl. Acad. Sci. U.S.A.*, 98(19):10533–10540, 2001. doi: 10.1073/pnas.191266498. URL `http://www.pnas.org/content/98/19/10533.abstract`.

[10] Jeremy O. Richardson, Stuart C. Althorpe, and David J. Wales. Instanton calculations of tunneling splittings for water dimer and trimer. *J. Chem. Phys.*, 135(12):124109, 2011. doi: 10.1063/1.3640429. URL `http://link.aip.org/link/?JCP/135/124109/1`.

[11] Krzysztof Szalewicz, Claude Leforestier, and Ad van der Avoird. Towards the complete understanding of water by a first-principles computational approach. *Chem. Phys. Lett.*, 482(1–3):1–14, November 2009. ISSN 0009-2614. URL `http://www.sciencedirect.com/science/article/pii/S0009261409011336`.

[12] Yimin Wang and Joel M. Bowman. Towards an ab initio flexible potential for water, and post-harmonic quantum vibrational analysis of water clusters. *Chem. Phys. Lett.*, 491(1-3):1–10, May 2010. ISSN 0009-2614. URL `http://dx.doi.org/10.1016/j.cplett.2010.03.025`.

[13] Robert Bukowski, Krzysztof Szalewicz, Gerrit C. Groenenboom, and Ad van der Avoird. Predictions of the properties of water from first principles. *Science*, 315(5816):1249–1252, 2007. doi: 10.1126/science.1136371. URL `http://www.sciencemag.org/content/315/5816/1249.abstract`.

[14] Jeremy O. Richardson and Stuart C. Althorpe. Ring-polymer instanton method for calculating tunneling splittings. *J. Chem. Phys.*, 134(5):054109, 2011. doi: 10.1063/1.3530589. URL `http://link.aip.org/link/?JCP/134/054109/1`.

[15] Yimin Wang, Bastiaan J. Braams, Joel M. Bowman, Stuart Carter, and David P. Tew. Full-dimensional quantum calculations of ground-state tunneling splitting of malonaldehyde using an accurate ab initio potential energy surface. *J. Chem. Phys.*, 128(22):224314, 2008. doi: 10.1063/1.2937732. URL `http://link.aip.org/link/?JCP/128/224314/1`.

[16] Massimo Marchi and David Chandler. Path-integral calculation of the tunnel splitting in aqueous ferrous–ferric electron transfer. *J. Chem. Phys.*, 95(2):889–894, 1991. doi: 10.1063/1.461096. URL `http://link.aip.org/link/?JCP/95/889/1`.

[17] Mariko Takahashi, Yumiko Watanabe, Tetsuya Taketsugu, and David J. Wales. An ab initio study of tunneling splittings in the water trimer. *J. Chem. Phys.*, 123(4):044302, 2005. doi: 10.1063/1.1954768. URL `http://link.aip.org/link/?JCP/123/044302/1`.

[18] Jeremy O. Richardson. *Ring-Polymer Approaches to Instanton Theory.* PhD thesis, University of Cambridge, May 2012.

[19] Jeremy O. Richardson, David J. Wales, Stuart C. Althorpe, Ryan P. McLaughlin, Mark R. Viant, Orion Shih, and Richard J. Saykally. Investigation of terahertz vibration–rotation tunneling spectra for the water octamer. *J. Phys. Chem. A*, (0), 2013. doi: 10.1021/jp311306a. URL `http://pubs.acs.org/doi/abs/10.1021/jp311306a`.

[20] Adam Reid. Quantum tunnelling splittings from ring-polymer instanton theory. CPGS Report (Department of Chemistry, Cambridge), 2011.

[21] Richard P. Feynman, Albert R. Hibbs, and Daniel F. Styer. *Quantum Mechanics and Path Integrals.* Dover Publications, 2005.

[22] Mark E. Tuckerman. Path integration via molecular thermodynamics. Lecture Notes (Dept. of Chemistry and Courant Institute of Mathematics, New York), 2002.

[23] R. Shankar. *Principles of Quantum Mechanics.* Springer-Verlag, 1994.

[24] Jeremy O. Richardson. private communication, Nov 2012.

[25] Robert M. Shields, Berhane Temelso, Kaye A. Archer, Thomas E. Morrell, and George C. Shields. Accurate predictions of water cluster formation, (H2O)n=2–10. *J. Phys. Chem. A*, 114(43):11725–11737, 2010. doi: 10.1021/jp104865w. URL `http://pubs.acs.org/doi/abs/10.1021/jp104865w`.